Obtaining highly transferable parameters for empirical tight-binding simulations: From pure materials to polytypic heterostructures and dilute alloys

Anh-Luan Phan,[1,*] Daniele Soccodato,[1] Alessandro Pecchia,[2] Alessia Di Vito,[1] and Matthias Auf der Maur[1]

[1] *Department of Electronic Engineering, University of Rome Tor Vergata, Via del Politecnico 1, 00133 Rome, Italy*
[2] *CNR-ISMN, Area della Ricerca di Roma 1, 00010 Rome, Italy*

(Dated: February 28, 2026)

The tedious parameterization process remains a key bottleneck hindering broader adoption of the empirical tight-binding method. Here, we discuss the challenges and requirements of finding parameters for Slater-Koster-based empirical tight-binding schemes, and explain the shortcomings of the parameterization procedures commonly used in the literature. We then propose our way to address these challenges, through the presentation of an open-sourced parameterization toolbox that breaks up the task into several, incremental stages. The prototype of our toolbox is tailored especially to deal with a recently proposed, highly transferable scheme, but can be easily adapted to any Slater-Koster-based scheme. A case study of fitting GaN parameters is considered. Remarkably, the obtained GaN parameter set shows high transferability when being applied to various contexts: from simple zincblende or wurtzite bulk cases, to polytypic heterostructures and even the cases of highly mismatched alloys in their dilute limits. This confirms the effectiveness and robustness of our parameterization approach.

Keywords: empirical tight-binding, parameterization, transferability, nitride, polytype, highly mismatched alloy

I. INTRODUCTION

Since the seminal work of Slater and Koster in 1954 [1] that set a firm ground for the practical usages of the empirical tight-binding (ETB), this method has served as a cornerstone of semiconductor modeling for decades. Because of its wide range of applications, there are many flavors of ETB that focus on different aspects of the material and device simulations. Comprehensive topical reviews discussing the method, different flavors as well as their applications can be found for example in [2–6]. In the context of this work, by "ETB" we refer to those which are highly specialized on accurately describing the electronic and optical properties of the semiconductor materials. The ETB offers a computationally efficient framework for predicting electronic and optical properties of nanostructures with atomistic precision. Its utility spans a diverse range of systems such as quantum dots [7], nanowires [8], quantum wells [9], random alloys [10] and even hybrid perovskites [11]. In these systems, conventional continuum models like $k \cdot p$ theory often fall short in accurately capturing atomic-scale effects, particularly in complex geometries or materials with significant local variations. While higher-accuracy methods like density functional theory (DFT) can address these limitations, they become computationally intractable for large-scale nanostructures. The ETB, therefore, strikes a crucial balance, providing atomistic resolution with significantly reduced computational cost compared to DFT, making it ideal for simulating large and complex systems where $k \cdot p$ is inadequate and DFT is too expensive. However, the ETB's accuracy critically depends on the parameter set's quality, requiring careful balancing of competing demands: accurate reproduction of bulk band structures, faithful capture of strain-induced deformations, and robust transferability across various situations such as different crystal phases, heterostructures and alloys.

As an empirical method, one of the main bottlenecks of the ETB scheme is the availability of large databases of transferable parameter sets for various materials of interest. In fact, every ETB implementation requires its own parameter sets, that should be compatible with the underlying physics of that scheme. Therefore, if researchers want to broaden the application range of a certain ETB scheme, the task of parameter-fitting (or also referred to as parameterization procedure) is unavoidable. In addition, the accuracy and transferability of ETB calculations is believed to depend heavily on the quality of the fitting parameters [7]. However, the parameterization procedure is not as trivial as it seems to be at first glance, especially for more sophisticated ETB schemes, which typically need a large number of parameters. Here it is quite relevant to mention the Wannier construction and interpolation - a popular approach to build the effective tight-binding models in which the electronic states from *ab-initio* calculations are used to construct the (maximally localized) Wannier functions, which in turn are used as the basis set to calculate the physical properties of the given structure (for a topical review, see [12]). Being different in the philosophy, the ETB does not explicitly know its basis functions, but cares only about the coupling parameters between them and how these coupling parameters change as the atomistic structure changes, which is also modeled by some other parameters (see Section II A). The ultimate goal of the ETB parameterization, simply speaking, is to find the best values of these parameters.

* anh.luan.phan@uniroma2.it

Traditional parameterization approaches usually try to fit only the features of the band structure, which may not always lead to highly transferable parameter sets [13]. The lack of a standardized and easily-implementable parameterization procedure has hindered the widespread adoption of advanced ETB schemes, which in general require much more fitting parameters, limiting their impacts on the research community. Thus, the open availability of such a parameterization procedure has far-reaching implications for the computational modeling community. It facilitates the use of sophisticated ETB methods, enabling researchers to harness the power of these tools for studying semiconductor alloys and heterostructures of interest. In this spirit, one of the key goals of this article is to delineate an easy-to-implement, easy-to-use and computationally effective parameterization procedure that can be tailored to suit any ETB scheme based on the Slater-Koster framework.

This work aims to address the above deficiencies by proposing a strategy for performing the ETB parameterization accompanied by an open-sourced toolbox of scripts. Our strategy combines the strengths of multi-objective optimization algorithms with a physically motivated staging approach. The process is divided into multiple stages, each focused on a specific subset of parameters and DFT targets. Stage 1 starts with estimating the parameters for a minimal sp^3 basis and then for a larger $sp^3d^5s^*$ basis, following the recipes in [14] and [15], respectively. These estimated values serve as a reasonable initial guess and help to determine the energy bounds for the optimization in Stage 2, where the multi-objective optimization algorithm tries to find the best fit of the onsite and hopping parameters to reproduce both the band energies and the wavefunction characters of the unstrained zincblende configuration. Stage 3 is similar, but the band offset's variation and the parameters related to bond-length dependencies are fitted instead. Finally, in stage 4 the parameters related to higher-order strain corrections are obtained. This staging approach reduces the dimensionality of the optimization problem at each stage, making it more tractable and less computationally demanding. We also utilized a set of physically motivated constraints and regularization techniques to ensure the physical meaningfulness and transferability of the resulting parameter sets.

The effectiveness of our parameterization strategy is then demonstrated through a case study of GaN, a wide-bandgap semiconductor that can exist in both wurtzite and zincblende phases [16]. By applying our method to parameterize zincblende GaN, we obtained a highly transferable parameter set that is able to reproduce the DFT bulk band structures of both crystal phases with sufficient fidelity. Moreover, we will demonstrate that our GaN parameter set is also applicable to the more complex cases of polytypic heterostructures and highly mismatched alloys (HMAs), reproducing results comparable to corresponding DFT calculations. This successful parameterization validates the robustness of our approach and highlights the importance of having an effective and easy-to-use parameterization procedure for the wider adoption of advanced ETB schemes. By lowering the barrier to entry, our work aims to accelerate the discovery and design of novel materials and devices, contributing partly to the searches for technological breakthroughs in fields such as material science and electronic engineering.

This paper is structured as follows. In Section II we briefly present the theoretical foundation of the ETB method, mentioning the landscape of the various ETB schemes in the literature and then focus on the requirements and challenges of the parameterization procedure; Section III is a detailed description of our parameterization strategy, using GaN as an example; the validations of the obtained GaN parameter sets are then exhibited in Section IV to show the effectiveness of our approach; finally, Section V is devoted to the conclusions and outlooks.

II. THEORETICAL BACKGROUND

A. Basic idea of ETB

The tight-binding method's fundamental premise involves expanding a single-electron wavefunction $|\psi\rangle$ as a linear combination of localized atomic-like orbitals $\{|\phi_{\alpha,i}\rangle\}$ associated with unit cell atoms. Here, i denotes the atom index while α encapsulates the orbital's quantum numbers (n, l, m, s). Namely,

$$|\psi\rangle = \sum_{(\alpha,i)} c_{\alpha,i}|\phi_{\alpha,i}\rangle, \tag{1}$$

where (in the position representation) the basis functions have the form:

$$\langle\vec{r}|\phi_{\alpha,i}\rangle = R_{(n,l),i}(\vec{r})Y_{(l,m)}(\theta,\varphi) \tag{2}$$

with $Y_{(l,m)}(\theta,\varphi)$ being the well-known spherical harmonic functions and $R_{(n,l),i}(\vec{r})$ being some highly localized radial functions. The choice of the localized atomic-like orbitals is natural because one wants the atomistic resolution of the system, in contrast to the choice of extended Bloch functions in continuum models like $k \cdot p$. The above basis set can always be orthogonalized via the Löwdin's procedure [17]. Then, the single-electron Hamiltonian can be written as:

$$H = \sum_{(\alpha,i)} |\phi_{\alpha,i}\rangle E_{\alpha,i}\langle\phi_{\alpha,i}| \quad + \sum_{\substack{(\alpha,i),(\beta,j)\\(\alpha,i)\neq(\beta,j)}} |\phi_{\alpha,i}\rangle\ V_{(\alpha,i)}^{(\beta,j)}(\vec{d}_{ij})\langle\phi_{\beta,j}|. \tag{3}$$

If the basis set is known *a priori*, the integrals $E_{\alpha,i}$ and $V_{(\alpha,i)}^{(\beta,j)}$ can be computed, in principle. However, we try to avoid this task in practical simulations because it is

rather difficult and tedious [1]. More pragmatically, one may temporarily put aside the explicit forms of the basis orbitals to treat these integrals as *empirical* values being fitted to higher-accuracy reference targets from the experiments or more sophisticated calculation methods such as the *ab initio* calculations, hence the name "*empirical* tight-binding". Within the ETB formalism, the parameters $E_{\alpha,i}$ are characterized as on-site parameters, whereas $V_{(\alpha,i)}^{(\beta,j)}$ are classified as off-site parameters - alternatively denoted as interatomic coupling or hopping terms - if $i \neq j$. According to the two-center approximation, these off-site parameters are defined as functions of the magnitude and orientation of the interatomic displacement vector $\vec{d}_{ij}$ connecting the atomic sites. For the case $i = j$, the $V_{(\alpha,i)}^{(\beta,i)}$ correspond to intra-atomic couplings between distinct orbitals localized on the same atom. Such contributions are usually neglected in conventional implementations of the ETB framework.

Once we have all the necessary parameters, the ETB Hamiltonian in Eq. 3 can be represented numerically in the form of a square matrix of the size equal to the number of orbitals in the simulation cell. Diagonalizing this matrix provides the eigenvectors (in terms of $c_{\alpha,i}$ coefficients) and the corresponding eigenenergies. However, even the Hamiltonian in Eq. 3 is not really convenient to work with, and thus requires some more simplifications to make it more practical for realistic simulation tasks. A general framework for this purpose was introduced by Slater and Koster in their seminal article [1] in 1954.

In addition to treating the normal bulk case, it is also required that the ETB is capable of accounting for various strain effects because of its significant impacts on the electronic and optical properties of the structures. In fact, in most heterostructures strain is large enough to critically influence the electronic states. From an atomistic point of view, strain is related to the displacement of atoms from their relaxed lattice positions, thus possibly breaking symmetries of the crystal and changing the crystal potential around each atom. Compared to $k \cdot p$, where strain can be treated with relative ease based on the Pikus-Bir strain correction to the Hamiltonian [18], which only needs the strain tensor related to the deformation of the Bravais lattice, in ETB strain is encoded in the atomic positions. Therefore, strain-related corrections to the Hamiltonian matrix elements, in principle, should be formulated as functions of atomic coordinates. Only in the case of sp^3 parameterizations, an approach based on Pikus-Bir corrections has been described [19]. In essence, this means that extra corrections have to be added to the ETB Hamiltonian matrix via adjusting the existing ETB parameters of the ideal zero-strain case and/or introducing additional parameters.

A variety of ETB schemes based on Slater-Koster framework [1] have been proposed along with their individual strain treatments. Beside the ways to account for strain, these schemes are essentially distinguished from each other in the basis set (from sp^3 to $sp^3d^5s^*$), in the orthogonality of the basis set, and in how many nearest-neighbor shells are considered, etc. Some notable ETB schemes proposed in the literature for common group-IV and III-V semiconductor materials are listed in Tables III and IV in Appendix A. The tables compare these ETB schemes in terms of important characteristics including strain-related ones. From these tables, one can see that generally the more sophisticated strain treatment the model has, the larger number of fitting parameters it would require. Most of the schemes listed, including the widely used scheme by Jancu et al. [15] (hereafter referred to as the "Jancu scheme"), take into account only some aspects of strain effects, except the most recent one proposed by Tan et al. [20] (hereafter referred to as the "Tan scheme"). As shown in a thorough discussion in [10], the Tan scheme is superior to the Jancu scheme in terms of the transferability at the price of a much larger number of fitting parameters than any ETB scheme previously proposed. This leaves us with the dilemma between the desire to maintain the quality of the ETB calculations and the demand to find a large number of fitting parameters having high degree of transferability.

B. Parameterization's requirements and challenges

The ETB methodology fundamentally seeks to circumvent direct computation of complex atomic orbital integrals by instead fitting parameters to experimental data or high-accuracy theoretical results. The fitting, or parameterization procedure, is done with some optimization algorithm. The most obvious difficulty one faces during the parameterization process is the large number of parameters that need to be taken into account, leading to a complex optimization landscape. As shown in Tables III and IV in Appendix A, an ETB scheme like the Jancu scheme using the $sp^3d^5s^*$ basis set and the first-nearest-neighbor approximation will require ~ 50 parameters for each binary material. For its amended versions [21–24] or other more sophisticated schemes [20, 25–27], this number inflates even more. The Tan scheme [20], with all of its complications, requires a full set of more than 150 parameters for a binary material. This leads to some requirements on the choice of the optimization algorithm. With an increasing number of parameters to be fitted at the same time, the configuration space in which the optimization algorithm has to search for the best fit becomes higher in dimensionality. This, on one hand, invalidates the use of brute-force approaches, on the other hand, poses a high risk of being stuck in some local extrema that give physically meaningless fits. Thus, the numerical efficiency of the algorithm and the robustness of the obtained fit are two important requirements that need special care when performing the parameterization.

It has been well recognized in the community that, apart from the sophistication of the ETB scheme itself, the quality of the accompanying parameter sets also has

an important role in assuring the accuracy of ETB calculations [7]. High-quality parameter sets demonstrate transferability – maintaining accuracy when applied to different physical quantities (e.g. optical properties) or when transferred to different structures made of the same constituents (e.g. from pure bulk to alloys or heterostructures, or between different crystal phases, ...). For the former, the targets to be fitted to (which are usually taken from DFT) in principle should include the features of the band structures (e.g. band dispersions, effective masses, band splittings, ...) as well as those of the corresponding wavefunctions (e.g. contributions from different orbitals). Traditional parameterization approaches often focus exclusively on band structure reproduction, whereas the wavefunction-related features were usually ignored, or at most only considered as a post-check after the parameterization as in [15]. This band-structure-only approach introduces ambiguity, as multiple parameter sets may reproduce band features equally well while differing dramatically in physical validity [28]. More specifically, by analyzing the case of MoS_2 in [13], the authors of that work concluded that matching only to the band structure is not enough to ensure that the ETB can accurately reproduce the optical response, and matching to the wavefunctions in the parameterization is also needed. Incorporating wavefunction characteristics as primary optimization targets from initial stages helps to resolve this ambiguity and at the same time improve optimization efficiency. The transferability of the obtained fit will also be enhanced especially when calculating the quantities that involve the wavefunctions like the optical response.

In addition, the best way to ensure the parameter sets can work well for different structures is to include more profiles (different materials, strains, crystal phases, ...) into the fitting. By design, most of the ETB schemes mentioned in Tables III and IV in Appendix A consider each pure semiconductor material as a separate fitting problem. For example, after having obtained the parameter set for GaAs, one continues fitting e.g. GaSb separately without imposing any constraint on the parameters related to the common Ga ion, though some authors tried to keep the values of onsite energies of the common ions in different materials close to each other. This is not the case in the Tan scheme because the bare onsite parameters of any ion are fixed no matter the material. Consequently, the parameter sets of all binary materials are weakly coupled together by these bare onsite parameters and in principle these materials should not be fitted separately but simultaneously to ensure the transferability. An analogous argument applies for including different crystal phases of the same material. In summary, an ideal ETB parameterization procedure should be designed so that it is able to take the wavefunction-related features into account and work with multiple target profiles at the same time, which will demand a significant amount of computational effort for every iteration of the optimization algorithm. This once again emphasizes why an efficient and robust parameterization procedure is in need.

Different from the above traditional approach which is band-structure-only and not multi-profile, the Tan ETB scheme is backed by a more advanced strategy called DFT mapping method [29, 30] developed by the same research group. Basically, in this method the explicit analytical forms of the radial parts of the atomic-like basis functions s, p, d are chosen in advance (e.g. Slater-type orbitals, Gaussian functions or something else) with some adjustable parameters. For a given set of these adjustable radial-function parameters, the basis functions are orthogonalized using Löwdin's procedure [17], and the orthogonalized basis set is then used to build the tight-binding Hamiltonian matrix. In this process, the various integrals $E_{\alpha,i}$ and $V_{(\alpha,i)}^{(\beta,j)}$ must be calculated numerically. The tight-binding Hamiltonian matrix is diagonalized to obtain the tight-binding energies and wavefunctions (represented in the orthogonal basis set above). One then calculates the loss function that characterizes the matching between the results from tight-binding and those from the referenced DFT. The total loss function is a weighted sum of three contributions, stemming from the comparisons of the band energies, the effective masses and the wavefunctions [31]. The total loss function is used by the optimization algorithm to decide how to modify the adjustable radial-function parameters in the next iteration. The parameterization is terminated when this loss function converges to a minimum. Once the atomic-like basis set is available, the ETB parameters of the ETB scheme can be deduced.

The power of this DFT mapping strategy has been demonstrated by the simulation results in [10, 20, 29, 30]. However, problems arise for other researchers wanting to utilize this strategy to extend the parameter database to other materials. The most obvious hurdle is the computational effort this method would require. For example, one would need to numerically calculate the ETB integrals, which is a tedious task and should be avoided in general according to the philosophy of Slater-Koster framework. Besides, other minor steps such as orthogonalizing via the Löwdin procedure, diagonalizing the Hamiltonian matrix and projecting the DFT wavefunctions onto the atomic-like basis functions, etc ... are also not lightweight in computation. All of these steps need to be done for each trial parameter set, thus requiring high-performance computing facilities, otherwise the computational time would be excessively long. On the other hand, there is only a single loss function to be minimized (single-objective optimization). Obviously, the value of the total loss function will change depending on the weight assigned to the three contributing loss functions, impacting the fitting procedure. In other words, by setting the weights we inject our bias on how one quantity is more important than the others, and on what the best fit should be, i.e., changing the values of the weights gives different best fits. Also note that the band energies, the effective masses and the wavefunctions are distinct in

the physical nature, and there is no *a priori* guideline to determine the relative magnitudes of the corresponding weights. Last but not least, to the authors' knowledge no standalone code implementation of the DFT mapping method has been made public so far. That said, if other researchers would like to perform the parameterization on their owns, they will need to implement the method themselves from scratch, which is a difficult task due to all of the mentioned complexities of the DFT mapping strategy. Therefore, a simplified, more user-friendly and more computationally efficient alternative that retains the main spirit of the DFT mapping method is desired. In the next section, we will present such a parameterization strategy developed in our research group that we applied in practice for the Tan scheme. It is, however, straightforward to modify this strategy for any other ETB scheme based on the Slater-Koster framework.

III. THE PARAMETERIZATION STRATEGY

Our approach proposed here still follows the same idea of matching both band energies and wavefunctions (note that the effective masses are just characteristics derived from the band dispersions) and fitting multiple profiles at the same time. However, there are some different features that make our approach more pragmatic for practical use. Firstly, we fit directly the ETB parameters and not the parameters of the radial functions, that is, we neither need to find an explicit basis set nor calculate the ETB integrals to build the Hamiltonian matrix. Secondly, we consider the band energies and the wavefunctions as two separate objectives to be fitted instead of summing their loss functions together in a weighted manner. This makes the parameterization become a multi-objective optimization problem and we used the multi-objective genetic algorithm (MOGA) supplied by the Global Optimization Toolbox [32] of MATLAB® [33]. In this situation there is not only a single best fit, instead the algorithm will try to find a collection of fits called Pareto front in which one objective cannot be improved without sacrificing the other objectives. At the end of the parameterization procedure, it is the user's responsibility to pick out the most suitable one among the Pareto fits. The wavefunctions from ETB and DFT are compared in terms of orbital-character contributions (i.e., the squared modules of the expansion coefficients) of *s*-, *p*-, *d*-symmetry orbitals of cation and anion. Comparing the squared modules of the expansion coefficients saves us from the cumbersome wavefunction-phase matching in the DFT mapping method.

In order to cope with the large number of fitting parameters, the whole parameterization procedure is divided into stages so that the parameter set is fitted portion by portion, in the order from the most important to the least important parameters, instead of fitting all of them at the same time. This helps reduce the dimensionality of the configuration space that the algorithm needs to handle, thus enhancing the efficiency, robustness, and portability. In the following, to make the descriptions of the stages more intuitive, we take the parameterization of GaN as an example. Also, we visualize the workflow of our strategy by a schematic flowchart in Fig. 1, hoping this can make it easier for the readers to follow.

The DFT targets need to be prepared beforehand. Producing high-quality DFT results is also not easy and should be discussed on its own. The DFT targets we used in this work were prepared using the commercial software QuantumATK [34] (see Appendix B for more details about our preparation of the DFT targets). The ETB calculations (using either the Jancu scheme or the Tan scheme) was performed using our UPTIGHT code, which is an integrated module in the multiscale simulation software TiberCAD [35, 36]. Given all the necessary DFT data, we proceeded to fit an ETB parameter set for GaN that is compatible with the Tan scheme as follows.

Stage 1: Estimating Jancu-like parameters' values

It is obvious that for materials in zincblende phase without any external strain, due to lattice symmetries a large number of parameters in the Tan scheme become irrelevant to the results and the Tan scheme is exactly equivalent to the Jancu scheme in the appearance. Therefore, we can start by fitting these Jancu-like parameters to the unstrained zincblende GaN target. However, before that we need reasonable estimations for the ranges of these parameters. The best way to do this is to first use the minimal basis set sp^3 and then include more orbitals (s^* and d). The reason is that for sp^3 basis set there are simple expressions relating directly the values of the DFT band energies for zincblende structure at some critical k-points (e.g. Γ and X points) to the parameters. We followed the steps described in Subsection 3a of [14] to deduce the onsite energies of s and p orbitals and the hopping parameters between them, as given in Table V in Appendix C for demonstration (spin-orbit coupling was temporarily ignored at this step). Because the orbital energies of isolated atoms (here Ga and N atoms) were used as part of the inputs, the onsite energies in this table seem to have reasonable values relative to each other. Note that, however, onsite energies are always determined up to some constant so that shifting all the onsite energies up or down the same amount of energy does not change the band dispersions but only the band offset when compared to other materials. It should be emphasized that this small parameter set already gives a reasonably good agreement for the valence band dispersions and the band gap of unstrained zincblende GaN, as shown in Fig. 2

Next, we extended the basis set to $sp^3d^5s^*$ and estimated other parameters in a similar way as described by Jancu et al. in Subsection IV.A of [15]. Namely, we first calculated the so-called $E_{\text{unit}} = (h/a)^2/(2m_0) \approx 7.3252$ eV where $a = 0.4531$ nm is the lattice constant of un-

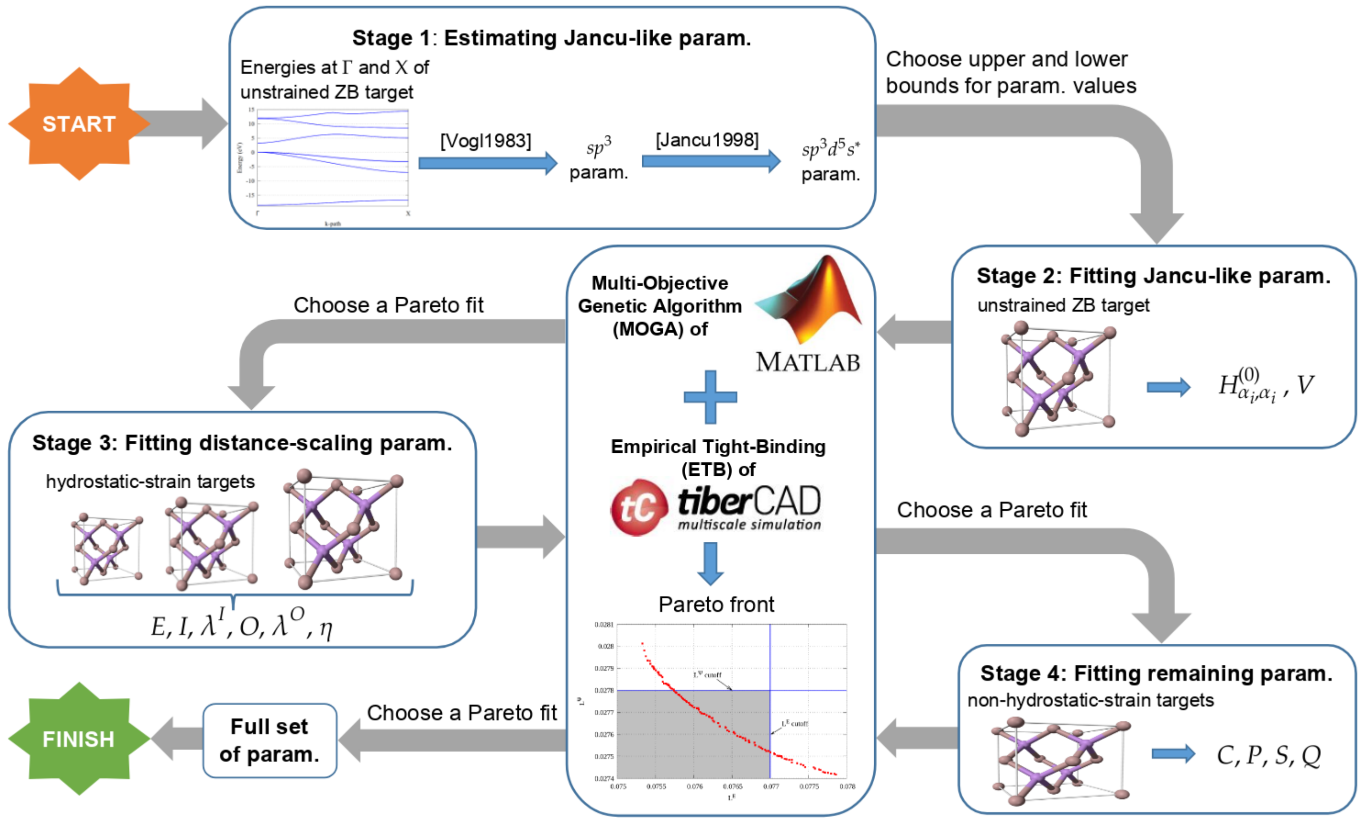

FIG. 1. Schematic flowchart of our parameterization procedure. “Param.” stands for “parameter(s)”. The citations [Vogl1983] and [Jancu1998] in Stage 1 refer to the papers [14] and [15], respectively. Here we borrowed the notations in [20] for the ETB parameters in the Tan scheme. The images of zincblende lattices are attributed to Benjah-bmm27 - Own work, Public Domain, https://commons.wikimedia.org/w/index.php?curid=2146789.

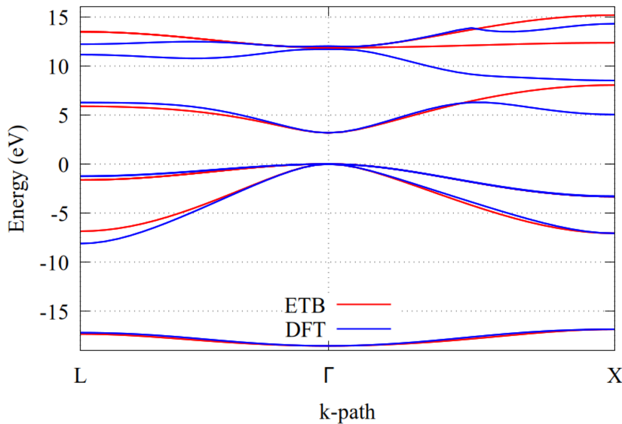

FIG. 2. The ETB band structure (red lines) of unstrained zincblende GaN produced with the sp^3 parameters obtained following the steps in [14] in comparison with the DFT one (blue lines).

strained zincblende GaN at 300 K, m_0 is the mass of electron, h is the Planck’s constant. Then, the free-electron model’s parameters given in Table I of [15] were used as scaling factors multiplied with E_{unit} to estimate the values of the other Jancu-like parameters [37]. Since there are two onsite parameters E_{s_c} and E_{s_a}, we assigned their average value to E_s in that table so that E_d and E_{s^*} are calculated based on the differences with respect to E_s. Alternatively, assuming that zincblende GaN’s parameters are more or less similar to other zincblende III-V materials whose parameters were already given in [15], we can use those parameter sets to deduce more reasonable scaling factors than using those of the free-electron model. In essence, the goal of this stage is to have an idea about the reasonable energy ranges of the ETB parameters (approximately a few eV around the corresponding estimated values), thus helping the optimization algorithm to limit the search space in the next stage. Finally, we utilized the fact that the onsite energies can always be determined up to a constant to shift all the estimated onsite parameters an amount of energy so that $E_{s_c} = 0$. This, on one hand, is to keep the range of onsite energies not too large unnecessarily, on the other hand, to exclude one parameter, namely E_{s_c}, out of the fitting process in the next stage.

Stage 2: Fitting Jancu-like parameters

As mentioned previously, the spirit of our parameterization procedure is to utilize both the information from the DFT band dispersions $E_{n,k}^{\rm DFT}$ and the DFT wavefunctions $|\Psi_{n,k}^{\rm DFT}\rangle$ (n is the band index) . In particular, for the band dispersions we calculated all 8 valence bands and 6 lowest conduction bands (including spin-degeneracy) along the k-path $L-\Gamma-X$ in the Brillouin zone at some specific equally spaced k-points. The loss function L^E for band dispersions defined as the weighted sum of squared differences between the DFT energies with the corresponding ETB ones:

$$L^E=\sum_{n,k} w_{n,k}^E |E_{n,k}^{\rm DFT}-E_{n,k}^{\rm ETB}|^2. \qquad (4)$$

Here $w_{n,k}^E$ are the weights which are set manually to adjust the fitting quality at different zones, depending on the interest. Typically, we pay more attention to the band energies near the band gap and close to the critical k-points. Because we will never reach a perfect fit, prioritizing the important zones and compromising a bit of the fitting quality for unimportant zones can help the algorithm reach the convergence faster. For the wavefunctions, we assumed $|\Psi_{n,k}^{\rm DFT}\rangle$ can be expanded in terms of the atomic-like orbitals with s, p, d, ... symmetries as

$$\begin{aligned}|\Psi_{n,k}^{\rm DFT}\rangle = c_{n,k}^{s_c}|s_c\rangle + c_{n,k}^{p_c}|p_c\rangle + c_{n,k}^{d_c}|d_c\rangle +\\ c_{n,k}^{s_a}|s_a\rangle + c_{n,k}^{p_a}|p_a\rangle + c_{n,k}^{d_a}|d_a\rangle + \mathcal{O}\end{aligned} \qquad (5)$$

where $c_{n,k}^{\alpha_i}$ are the expansion coefficients of the corresponding orbitals on either cation ($i=c$) or anion ($i=a$) and $\mathcal{O}$ stands for the contributions from orbitals that lie much higher in energy. For the bands of interest $\mathcal{O}$ should be negligibly small and the squared modules of these $c_{n,k}^{\alpha_i}$ coefficients should add up to almost 1. Hence, for comparing the wavefunction composition we chose the Hellinger metric [38] as usually used for the comparison of probability distributions. The corresponding loss function L^Ψ for this is defined as:

$$L^\Psi=\sum_{n,k}\frac{w_{n,k}^\Psi}{\sqrt{2}}\sqrt{\sum_{\alpha_i}\left(\left|c_{n,k}^{DFT,\alpha_i}\right|-\left|c_{n,k}^{ETB,\alpha_i}\right|\right)^2}. \qquad (6)$$

It should be highlighted that since we used the modules of the $c_{n,k}^{\alpha_i}$ coefficients (which bear the probabilistic meaning) instead of the coefficients themselves, we did not need to worry about wavefunction-phase matching as when comparing them directly in [30]. Note that for s_c and s_a in the ETB, we also included the contributions of $c_{n,k}^{s_c^*}$ and $c_{n,k}^{s_a^*}$, respectively (see Appendix D for more discussions on this).

The task of the MOGA is to minimize the two objectives L^E and L^Ψ at the same time. In this stage, only the DFT profile of unstrained zincblende GaN was used and we had to fit approximately 30 Jancu-like parameters: the onsite orbital energies and the first-nearest-neighbor hopping parameters. The estimated values of these parameters in the previous stage may be supplied to MOGA as one of the initial guesses, whereas all the other guesses of the population were generated randomly within the energy ranges of a few eV around the corresponding estimated values. The algorithm tried to search for the Pareto points (each point is a distinct trial parameter set) in the objective space, as illustrated in Fig. 3. (See Appendix E for a trick to speed up the convergence.)

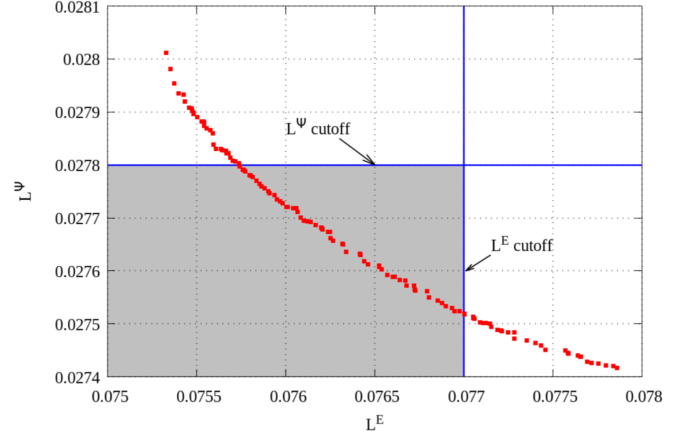

FIG. 3. An illustration of the optimization points (red points) in the two-dimensional objective space that form the so-called Pareto front (there are other non-Pareto optimization points that are not shown for the clarity). The two blue lines represent the cutoffs for L^E and L^Ψ to exclude uninteresting points and keep only Pareto points in the grey zone. These chosen points will be used as the initial guesses for the next cycle to speed up the convergence (see Appendix E for more details).

At the end of this stage we obtain a set of Pareto points from which the most suitable one (i.e., the most suitable parameter set) has to be chosen manually by examining the quality of the fitting of the band dispersions and wavefunction compositions. The human bias on prioritizing L^E or L^Ψ only comes into play at this decision step instead of being embedded from the beginning as by using the single-objective optimization algorithm, allowing us to have more choices depending on the desired trade-off between matching band energies and orbital compositions. Note that because the Jancu-like parameters are the most important portion of the parameter set, this stage is the most challenging and time-consuming stage of the whole procedure, thus requiring special care and patience.

Stage 3: Fitting distance-scaling parameters

Given the Jancu-like parameters from Stage 2, in this stage we fitted the parameters related to the distance dependencies of the onsite energies, hopping energies and band offset (for some discussions on why the band off-

set is involved in this stage, see Appendix F). The setup is similar to Stage 2 except that now we did not use the unstrained target profile but multiple profiles corresponding to the zincblende GaN under different hydrostatic strains, i.e. purely isotropic strains (from -6% to $+6\%$). In the Tan scheme, the distance scaling is modeled by exponential factors of the form $\exp(-\lambda \cdot \delta)$ where δ is the difference between the actual bond length and the reference bond length while λ are the fitting parameters characterizing how fast the energy couplings in Stage 2 "decay" with respect to the bond length. For a $sp^3d^5s^*$ scheme, at first we have 21 such λ^V (or η as denoted in [20])parameters corresponding to 21 first-nearest-neighbor hopping energies. Moreover, the Jancu-like onsite energies that we fitted in Stage 2 (denoted as $H^{(0)}_{\alpha_i,\alpha_i}$) are further decomposed into several terms (see Eq. 6 in [20]): the orbital-specific bare onsite parameters E_{α_i} due to the potential of atom i itself, the orbital-specific monopole contributions from its four nearest neighbors $\sum_{j=1}^{4} I_{\alpha_{i,j}} \exp(-\lambda^I_{\alpha_{i,j}} \cdot \delta)$ and the monopole contribution again to the variation of the band offset $\sum_{j=1}^{4} O_{i,j} \exp(-\lambda^O_{i,j} \cdot \delta)$. All of the these parameters have impacts on the Hamiltonian when the bond length changes, so we need to fit them all simultaneously. However, we can reduce the number of fitting parameters in this stage by making use of the above decompositions of $H^{(0)}_{\alpha_i,\alpha_i}$ to deduce the following 7 linear constraints:

$$
\begin{aligned}
E_{s_a} &= H^{(0)}_{s_a,s_a} + E_{s_c} + 4(I_{s_{c,a}} - I_{s_{a,c}}), \\
E_{p_a} &= H^{(0)}_{p_a,p_a} + E_{s_c} + 4(I_{s_{c,a}} - I_{p_{a,c}}), \\
E_{s^*_a} &= H^{(0)}_{s^*_a,s^*_a} + E_{s_c} + 4(I_{s_{c,a}} - I_{s^*_{a,c}}), \\
E_{d_a} &= H^{(0)}_{d_a,d_a} + E_{s_c} + 4(I_{s_{c,a}} - I_{d_{a,c}}), \\
I_{p_{c,a}} &= (H^{(0)}_{p_c,p_c} + E_{s_c} - E_{p_c})/4 + I_{s_{c,a}}, \\
I_{s^*_{c,a}} &= (H^{(0)}_{s^*_c,s^*_c} + E_{s_c} - E_{s^*_c})/4 + I_{s_{c,a}}, \\
I_{d_{c,a}} &= (H^{(0)}_{d_c,d_c} + E_{s_c} - E_{d_c})/4 + I_{s_{c,a}}.
\end{aligned} \tag{7}
$$

Therefore, 7 dependent parameters can be excluded. On the other hand, because we wanted to make our newly obtained GaN parameters compatible with the existing III-V parameter sets published in [20], the 4 E_{α_c} parameters of the Ga cation in that paper were reused here. To summarize, in this stage we only had to fit 36 (instead of 47) parameters in total: 5 I, 8 λ^I, O, λ^O and 21 η for the hopping energies. As a result, we will obtain a set of parameters that can now describe the zincblende GaN under either zero strain or hydrostatic strains.

Stage 4: Fitting the remaining parameters

Now we still have ~ 75 remaining parameters to fit to obtain a full set of ETB parameters compatible with the Tan scheme. Following the notations in [20], these include:

- $C_{\alpha_i\beta_i,j}$: characterizing the intracouplings between orbitals on the same ion i due to dipole or quadrupole components of its jth nearest neighboring ion's potential;
- $P_{\alpha_i\beta_j|m|}$, $S_{\alpha_i\beta_j|m|}$ and $Q_{\alpha_i\beta_j|m|}$: related to the averaged dipole (P and S) and quadrupole (Q) corrections to the intercoupling $V_{\alpha_i\beta_j|m|}$ (after the distance scaling) from the nearest neighboring ions of the coupling pair.

In a perfect zincblende crystal (i.e., no strain or only hydrostatic strains), the effects of these corrections will exactly cancel each other out, and thus there is no impact on the ETB calculations. That is why we were able to ignore them in the previous stages and isolate only the Jancu-like and distance-scaling parameters, consequently reducing the number of parameters that the optimization needs to handle simultaneously. This is the main spirit of dividing the whole parameterization strategy into stages. However, the impacts of C, P, S and Q, cannot be further decoupled from each other, so we had to fit them all at once in this stage. Note that many of these parameters were intentionally set to zero by Tan et al. in [20], but here we kept them all adjustable.

The setup is still similar to Stage 2, except that the target profiles are now for the non-hydrostatic strains of zincblende GaN such as uniaxial, biaxial or shear strains. Moreover, it can be reasonably expected that these dipole or quadrupole corrections are inferior to the monopole contributions and do not change the band dispersions drastically. Therefore, we can save some computational resources and boost the speed if, for the L^E loss function, we consider only the changes of the energy bands and the band edge splittings (if any) at the important critical k-points compared to the unstrained profile. This trick was also used by the authors of [20]. At the end of this stage, we obtained the full parameter set for GaN which is fully compatible with the Tan ETB scheme.

IV. A CASE STUDY OF GaN

The parameter set for GaN at room temperature, as shown in Tables VI and VII in Appendix C, was obtained by applying the strategy in Section III using only the target profiles of zincblende GaN and without any further refinement. Moreover, we utilized only part of the zincblende GaN band structures along the $L-\Gamma-X$ k-path instead of the full Brillouin zone. In this section, the quality and the transferability of this parameter set will be demonstrated via several typical test cases. The first and simplest test is to reproduce the full-Brillouin zone band structures of GaN in both zincblende and wurtzite phases. Upon passing the first test, the polytype transferability of this parameter set is further tested when applied to simulate a GaN polytypic heterostructure. Finally, we apply the parameters to perform preliminary investigations on the problems of III-V highly mismatched

alloys (HMAs) - namely GaPN, GaAsN and GaSbN - in both of their dilute limits.

A. GaN in zincblende and wurtzite phases

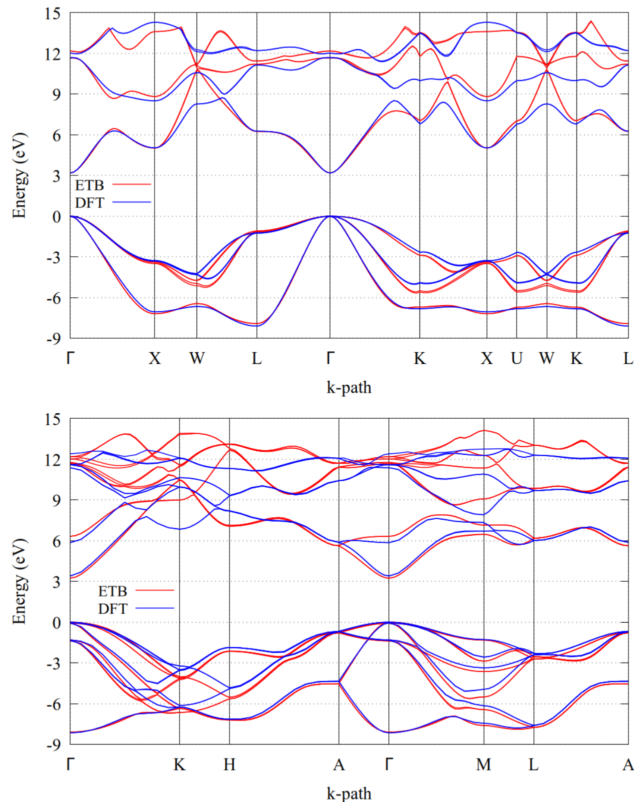

FIG. 4. The bulk band structures of GaN in zincblende (upper panel) and wurtzite (lower panel) phases at 300 K reproduced by our ETB parameters (red lines) and by hybrid-functional DFT (blue lines).

Fig. 4 shows the band structures of GaN in both zincblende and wurtzite phases given by our fitted parameters in comparison with those from the hybrid-functional DFT calculations. The quality of the ETB band dispersions for the case of zincblende is rather good over the whole Brillouin zone, apart from a region near W and K points, although the fitting considered only $L-\Gamma-X$ k-path. For the higher conduction bands, the fitting quality is lower as expected. However, noting the much larger energy scale of GaN compared to other III-V semiconductors, these higher conduction bands that are far away from the band gap are typically less relevant in practical applications.

Interestingly, the same parameter set can reproduce equivalently well the band structure of wurtzite GaN, demonstrating the polytypic transferability of our parameterization. Although the wurtzite band gap is slightly smaller than the DFT value and there are quite large discrepancies for the lowest conduction bands around K and H points, the general appearance of the ETB wurtzite band structure is in surprisingly good agreement with the corresponding DFT data, especially around the zone center. Moreover, our ETB parameters predicted that the valence band edge of the wurtzite phase to be 86 meV higher than that of the zincblende one, which is in excellent agreement with the experimental estimation of ~ 90 meV in [39]. The fact that the relative band offset between different crystal phases of the same material is a built-in feature instead of being added by hand is an advantage in simulating the heterostructures involving polytypism (see Section IV B).

In order to make a comparison in the effectiveness between our parameterization strategy and the DFT mapping method, we show in Fig. 5 the band structure of wurtzite GaAs using the parameters given by Tan et al. in [20], together with the corresponding hybrid-functional DFT calculation. It should be emphasized that the parameters in [20] were also obtained by fitting exclusively to the zincblende phase. It can be observed, that the degree of polytypic transferability is similar to our case, which substantiates the effectiveness of our parameterization strategy as a simplified alternative to the DFT mapping approach of [29, 30].

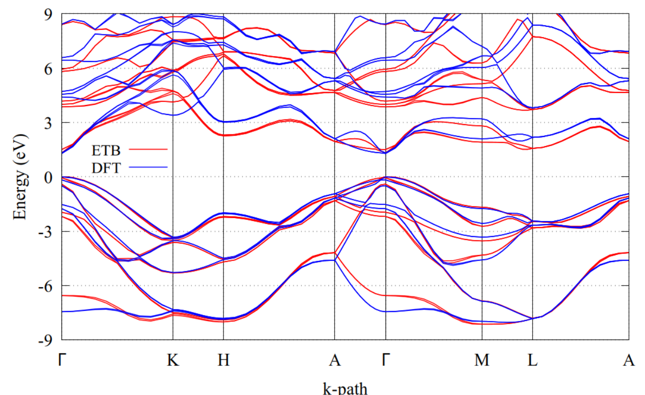

FIG. 5. The band structure of GaAs in wurtzite phase at 300 K reproduced by ETB with the parameters in [20] (red lines) and by hybrid-functional DFT (blue lines).

It is also worth mentioning that some researchers have made a lot of efforts to achieve such polytypic transferability, e.g. in [22, 40, 41]. Let us consider a case study of [41] where the authors tried to find such parameter sets for group-IV and non-nitride III-V semiconductors, including GaAs. They pointed out that the parameter sets for zincblende materials given by Jancu et al. in [15] are poorly transferable to wurtzite phase because some important physical effects are missing in the Jancu scheme. They then attempted to modify these parameter sets by simultaneously fitting both the zincblende and wurtzite band structures, still using the original Jancu scheme. However, they found that they had to compromise the fitting quality of the band structures away from the center of the Brillouin zone in both phases to better fit the

features at the center such as the direct gap and the effective masses of the conduction band, as illustrated in Fig. 1 in their Supplemental Material. From these facts we can conclude that the Tan scheme, thanks to its higher level of sophistication, appears to be superior to the Jancu scheme in achieving polytypic transferability.

B. Polytypic GaN superlattice

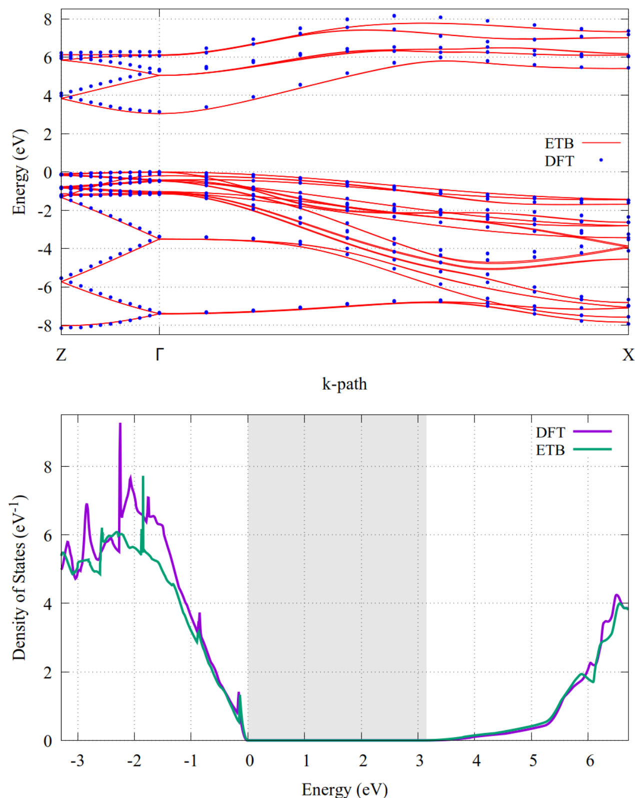

FIG. 6. The band dispersions (upper panel) and the total density of states (DOS) function (lower panel) of the considered GaN polytypic superlattice (stacking order ACBAB, see the text). The grey zone in the lower panel indicates the band gap.

Polytypic heterostructures, where the crystal phase (e.g., zincblende and wurtzite) rather than the chemical composition is spatially varying, have emerged as a promising platform for high-performance electronic and optoelectronic devices [42–44]. These structures increase the quality of the interfaces [45] compared to traditional material heterostructures by enabling atomically sharp interfaces with minimal defect densities.

Atomistic simulations of heterostructures involving polytypism require a unified framework to describe different crystal phases of the same materials. Traditional ETB schemes often lack polytypic transferability due to inconsistent parameterization of strain and orbital interactions across crystal phases, thus giving rise to both technical and conceptual problems. For example, to simulate the polytypic GaAs superlattices in [46] using the Jancu scheme, the authors had to use two distinct parameter sets for GaAs, one from [15] for the zincblende phase and one from [41] for wurtzite phase. As a consequence, this led to the conceptual question of uniquely assigning every atom to either zincblende or wurtzite. Moreover, it was not clear how the interfacial Ga-As intercouplings should be treated, and the physical justifications for the choice of taking linear combinations of the two bulk values as in [46] was not thoroughly discussed. Also, using different parameter sets requires us to put the relative band offset's value by hand.

We emphasize that all of the above problems will disappear if we use a single polytype-transferable parameter set to simulate the polytypic heterostructures. Motivated by this, we further test the polytypic transferability of our GaN parameter set by comparing the ETB results for a zincblende-wurtzite GaN superlattice with those of DFT. Note that the valence band offset of ~ 90 meV between wurtzite and zincblende phases is already encoded within the parameters. The chosen GaN polytypic superlattice has the stacking order $ACBAB$ in Ramsdell notation [47] (we follow the conventions used in [46]), which is the minimal combination between the zincblende phase (stacking order ABC along its [111] axis) and wurtzite phase (stacking order AB along its [0001] axis). A visualization of the unit cell of this minimal GaN polytypic superlattice with 5 Ga atoms and 5 N atoms is shown in the right panel of Fig. 7.

In Fig. 6 we compare the band dispersions and the density of states (DOS) function calculated by our ETB parameters with the corresponding DFT results. For the band dispersions, the ETB matches very well with DFT. The very slight underestimation of the superlattice's band gap is an inheritance from the fact that our parameters slightly underestimate the bulk band gap of GaN in wurtzite phase. The DOS functions in both DFT and ETB are obtained using the tetrahedron method in [48, 49] with the same k-space grid in the first Brillouin zone. The matching between the ETB DOS and the DFT DOS is fairly good, especially in the energy range near the band gap. However, at ~ 2 eV below the valence band edge, the DOS is underestimated by ETB. Next, we assess the projected DOS (PDOS) onto different atomic sites in a superlattice cell. The results are demonstrated in Fig. 7 along with a visualization of the corresponding unit cell. The ETB PDOS in the valence band is fairly good, while it deviates from the DFT results at high energies in the conduction band, as expected. More precisely, the ETB underestimates the PDOS on all Ga sites, while it overestimates the PDOS on the N sites. These differences, however, approximately cancel each other out so that the total DOS aligns to that of DFT even at higher energies as shown in Fig. 6.

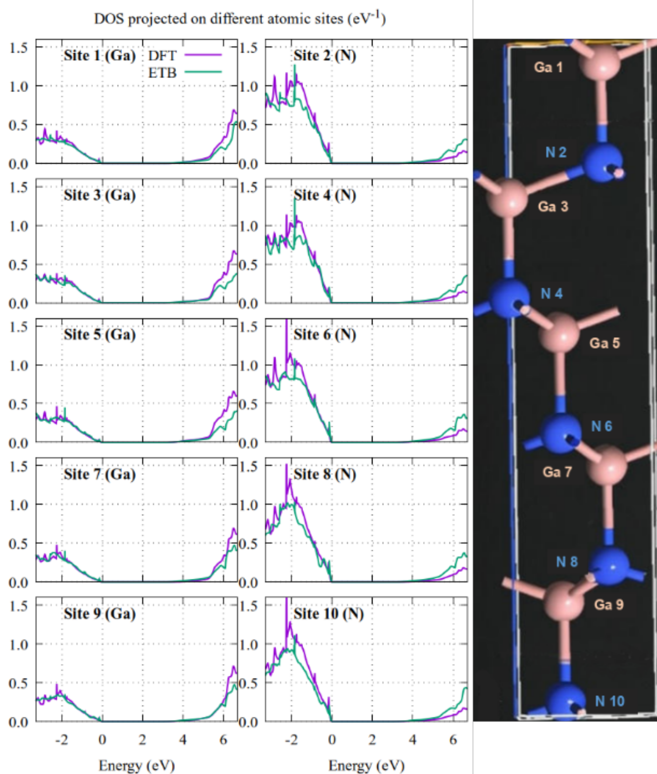

FIG. 7. The DOS projected (in eV^{-1}) on each atomic site in each period of the considered GaN polytypic superlattice (stacking order ACBAB, see the text).

C. Highly mismatched alloys in dilute limits

While conventional semiconductor alloys - whose constituent species are similar in terms of atomic size, ionicity and electronegativity - have been investigated intensively, the situation of HMAs - whose constituent species are distinctly differ in terms of the properties mentioned above - is more challenging from the experimental perspective [50]. HMAs have recently received growing attention from the community, mainly due to the advancements in preparation techniques that allow to grow such alloys over extended composition ranges [51, 52], and secondly to their unique electronic and optical properties, especially the large reduction of the band gap even in the dilute limit, i.e. at very low alloy compositions (usually a few percent) [53, 54].

Within the HMAs involving group-III and group-V elements, GaAs:N (zincblende GaAs diluted with N) is probably the most typical representative. In addition, GaP:N and GaSb:N are also of technological interest. Similarly, wurtzite GaN can be diluted with P, As or Sb. The peculiarities of the electronic band structure of HMAs compared to those of conventional III-V alloys require a good theoretical understanding of the changes in the band gap and/or band edges for potential applications. In this regard, most studies in the literature utilized the band anti-crossing (BAC) model [55–57] to quickly obtain phenomenological descriptions of these dilute HMAs, while other works are based on DFT calculations (see [50] and the references therein). Here we apply our ETB parameters for GaN - together with the already available parameters for GaP, GaAs, GaSb from [20] - to carry out preliminary investigations on three III-V HMAs including GaPN, GaAsN, GaSbN in both of their dilute limits using the supercell approach with a single impurity in each supercell. The details of the supercell simulations can be found in Appendix G. The alloy composition is of %N $\approx$ 1.56% for the cases of dilute-N zincblende Ga-V HMAs, while it is of %P/%As/%Sb $\approx$ 0.78% for the cases of wurtzite GaN diluted with P, As or Sb.

In Fig. 8 we present the calculated effective band structures of the dilute HMAs along with the band structures of the host materials overlaid on top for the sake of comparison. The simulated data show a reasonable chemical trend from P$\rightarrow$As$\rightarrow$Sb. In all the dilute-N cases (top panels in Fig. 8), the nitrogen impurity induces clear band splittings of the conduction band edge at Γ, which is consistent with the physical picture of the BAC model (see [58, 59] for GaP:N, [56] for GaAs:N, [60] for GaSb:N). In the opposite cases (bottom panels in Fig. 8), our ETB simulations predict modest changes in the conduction bands, while newly formed localized valence band edges appear, which originate from the P/As/Sb-impurity levels lying inside the GaN's band gap. These restructured valence band edges are responsible for the abrupt decreases of the optical band gap as observed in the photoluminescence spectra when just a small amount of P/As/Sb is incorporated into the wurtzite GaN (see Section III. F. of [50]).

For a quantitative analysis, we compared our results with published hybrid-functional DFT calculations and with experimental data. For the case of dilute Ga(P/As/Sb):N alloys, we compared only with DFT calculations using the same supercell configuration as ours, namely $Ga_{64}(P/As/Sb)_{63}$:N_1. Qualitatively, our effective band structures for GaP:N and GaAs:N in the top row of Fig. 8 compare well with the ones found in [61] (Fig. 2g) and [62] (Fig. 2a), respectively, while we did not find DFT effective band structures of GaSb:N. In Table I we present the band-gap reduction at the Γ-point resulting from our ETB calculations in comparison with both DFT and experimental data from the literature. Generally speaking, both ETB and DFT results deviate considerably from the experimental values. However, while the hybrid-functional DFT systematically overestimates the Γ-gap reduction of the dilute Ga(P/As/Sb):N alloys, in average our ETB gives values closer to the experimental data.

In the case of dilute GaN:(P/As/Sb) alloys, the most interesting feature is the abrupt band-gap reduction in the ultra-dilute regime (i.e., %P/%As/%Sb $<$ 1%) because it closely reflects the energetic position of the impurity P/As/Sb-level with respect to the valence band edge of GaN. Effective band structures calculated by hybrid-functional DFT for such ultra-dilute alloys are given in

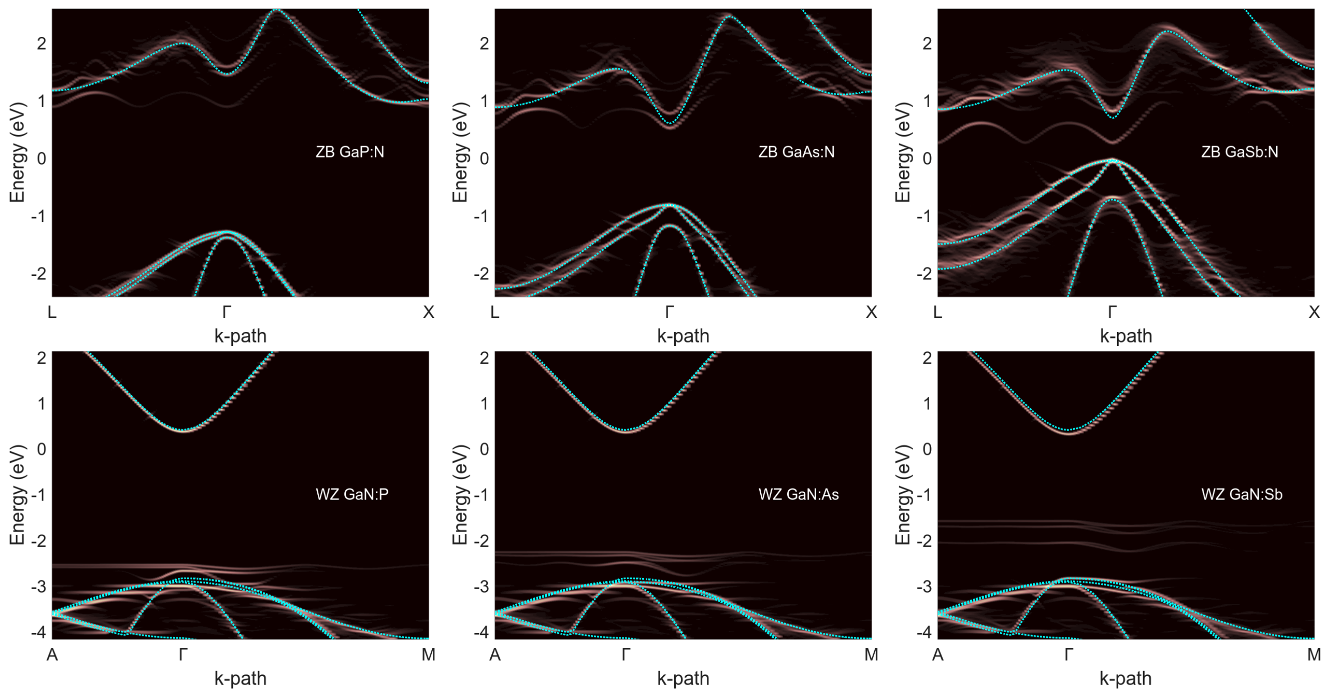

FIG. 8. The effective band structures (the black-to-pink color-map) of three HMAs in both dilute limits along with the band structure of the host material on top (the dashed cyan lines). For the labels, "ZB" and "WZ" stand for "zincblende" and "wurtzite", respectively. In each row of panels, the energy range is the same, so that one can easily compare the relative positions between the bands in different materials.

[63] (Fig. 6, first row). Once again, our ETB effective band structures in Fig. 8 (second row) closely resemble the DFT ones. In Table II we collect the band-gap reduction from our ETB in comparison with the DFT results from [63] and with experimental data. In this case, our ETB-predicted values agree well with the measured data, while the hybrid-functional DFT systematically underestimates the band-gap reductions.

TABLE I. Values (in eV) of the Γ-gap reduction for dilute zincblende Ga(P/As/Sb):N alloys (%N ≈ 1.56%).

	GaP:N	**GaAs:N**	**GaSb:N**
ETB	∼ 0.57	∼ 0.08	∼ 0.44
DFT	∼ 1.00 [61]	∼ 0.40 [62]	∼ 0.58 [64]
Exp.	∼ 0.70 [65]	∼ 0.24 [66]	∼ 0.32 [67]

TABLE II. Values (in eV) of the abrupt band-gap reduction for ultra-dilute wurtzite GaN:(P/As/Sb) alloys.

	GaN:P	**GaN:AS**	**GaN:Sb**
ETB	∼ 0.34	∼ 0.62	∼ 1.34
DFT	∼ 0.17 [63]	∼ 0.41 [63]	∼ 0.98 [63]
Exp.	∼ 0.50 − 0.54 [50, 68]	∼ 0.6 − 0.8 [50, 69, 70]	∼ 1.2 − 1.3 [50, 52, 71, 72]

From Tables I and II we can observe that the hybrid-functional DFT tends to lower the energetic positions of the newly formed band edge states, resulting in an under- and overestimation of the band gap reduction for the dilute GaN:(P/As/Sb) and Ga(P/As/Sb):N alloys, respectively. A similar issue has been observed by the current authors when calculating the band-gap variation of GaAsSb alloy using hybrid-functional DFT [73]. One possible cause could be the limited size of the supercells used in the hybrid-functional DFT calculations [74]. This would indicate that a correct description of random alloys would need much larger supercells, which from a computational point of view is more easily manageable with ETB than with hybrid-functional DFT.

V. CONCLUSIONS AND OUTLOOK

The ETB is one of the most commonly used methods for electronic and optoelectronic simulations. The sophisticated ETB schemes that are needed to obtain high accuracy and transferability for practical simulations require the availability of high-quality sets of ETB parameters. However, obtaining such high-quality parameter sets poses many challenges. Motivated by this, here we have presented a simplified and computationally efficient strategy for the ETB parameterization which retains the main spirit of a more complicated approach called the DFT mapping method [29, 30]. The code implementation of our strategy is open-sourced and can be easily used or modified by other researchers.

We applied our parameterization strategy to GaN as an example, obtaining a full set of ETB parameters that is compatible with the advanced ETB scheme of Tan et al. [20]. The effectiveness and validity of our strategy (as well as the obtained GaN parameters) were assessed via several typical test cases: the transferability between the two crystal phases zincblende and wurtzite, the transferability from bulk to a polytypic superlattice, and the transferability to highly mismatched alloys in dilute regimes. Although there are still some discrepancies, the overall results are very encouraging in the sense that they exhibit a similar degree of polytypic transferability as the parameters obtained via the more complicated DFT mapping method, suggesting our parameterization strategy is a viable alternative. Considering the modest DFT data available in our GaN example (only the band dispersions along $L-\Gamma-X$ and the wavefunction compositions at these three critical k-points), one can expect that the current discrepancies would be improved by enriching the DFT targets (e.g. full-zone band structures, wavefunction compositions at all critical k-points, wurtzite targets, etc ...).

We expect that our toolbox and procedure can help other researchers to perform the parameterization themselves and obtain high-quality parameter sets for the materials of interest, promoting the use of reliable but efficient atomistic simulations using ETB.

VI. CODE IMPLEMENTATION

Our ETB parameterization toolbox is available at [75]. This toolbox was tailored to work with the UPTIGHT code for the ETB calculations, which is also available freely at [76].

ACKNOWLEDGMENTS

The authors thank Dr. Yaohua Tan for the valuable discussions on his works [20, 30]. This work is supported by European Union's Horizon 2020 research and innovation programme under the Marie Skłodowska-Curie grant agreement n° 956548, project Quantimony. MAdM acknowledges support by the European UnionNextGenerationEU under the Italian National Center 1 on HPC-Spoke 6: 'Multiscale Modelling and Engineering Applications' MUR CUP: E83C22003230001.

Appendix A: A brief overview of the landscape of empirical tight-binding schemes

Tables III and IV together list some notable ETB schemes proposed in the literature for common group-IV and III-V semiconductor materials, comparing their strain-related characteristics.

TABLE III. Comparison of strain-related characteristics of various ETB schemes proposed in the literature. "Elem." stands for elemental materials (e.g. C, Si, Ge) while "binary" is for binary materials (e.g. GaAs).

Scheme	*Munoz et al. (1993) [77]*	*Tserbak et al. (1993) [78]*	*Mercer et al. (1994) [79]*	*Grosso et al. (1995) [80]*	*Jancu et al. (1998) [15]*	*Wang et al. (1999) [81]*	*Boykin et al. (2002) [25]*
Basis set	sps^*	sp	sp	sp	$spds^*$	sp	$spds^*$
Neighbor shells	first nearest	third nearest	first nearest	second nearest	first nearest	any	first nearest
Onsite shift			yes			yes	yes
Onsite splitting		p		p	d		yes
Intra-coupling			p-p				
Hopping correction	s^*-p					yes	
Distance scaling	Harrison law	Harrison law	other	Harrison law	Harrison law	other	Harrison law
Apply for strains	hydrostatic biaxial [001]	hydrostatic biaxial [001]	not clear	hydrostatic biaxial [001]	hydrostatic biaxial [001]	any	any
Parameters for		Si, Ge	Si	Si, Ge	C, Si, Ge, III-V	Si	GaAs, InAs
No. of parameters	binary: ~18	elem.: ~18	elem.: ~38	elem.: ~18	elem.: ~33 binary: ~52	elem.: ~60	binary: ~69

TABLE IV. Comparison of strain-related characteristics of various ETB schemes proposed in the literature (continued, end).

Scheme	*Jancu et al. (2007) [21]*	*Niquet et al. (2009) [26]*	*Boykin et al. (2010) [27]*	*Raouafi et al. (2016) [23]*	*Nestoklon et al. (2016) [24]*	*Tan et al. (2016) [20]*
Basis set	$spds^*$	$spds^*$	$spds^*$	$spds^*$	$spds^*$	$spds^*$
Neighbor shells	first nearest	first nearest	first nearest	first nearest	first nearest	first nearest
Onsite shift	yes	yes	yes	yes	yes	yes
Onsite splitting	yes	yes	yes	yes	yes	yes
Intra-coupling		yes	p-p, p-d, d-d	p-p, d-d	p-p, d-d	yes
Hopping correction						yes
Distance scaling	Harrison law	Harrison law	Harrison law	Harrison law	Harrison law	exponential
Apply for strains	hydrostatic biaxial [001], [111]	any	any	any	any	any
Parameters for	Ge	Si, Ge	Si	(Al,In)(As,Sb)	(Ga,In)(As,Sb)	Si, Ge, III-V (no N)
No. of parameters	elem.: ∼40	elem.: ∼46	elem.: ∼50	binary: ∼60	binary: ∼62	elem.: ∼100 binary: ∼150

Appendix B: Preparing the DFT targets

The DFT data needed in our parameterization procedure include the band structure targets and the wavefunction composition targets. The commercial software QuantumATK [34] (version U-2022.12-SP1) was exploited for the DFT calculations. The hybrid functional HSE [82] was chosen to model the exchange-correlation term. The mixing parameter α in the HSE functional was chosen so that the DFT band gap of the unstrained zincblende GaN matches the experimental value at room temperature, resulting in $\alpha = 0.39$; while the screening length was kept fixed at 0.11 Bohr^{-1}. A plane-wave basis set was chosen (implementation details in [34]), with a wavefunction cutoff of 35 Hartree. The PseudoDojo pseudopotentials [83] were used. The k-points sampling for the self-consistent calculation was set to a density of 4 Å in all directions. For the actual calculations, the Brillouin zone was sampled along the $L-\Gamma-X$ k-path, with 20 equally spaced points for each segment. We calculated the DFT band energies (8 valence bands and 6 conduction bands, including spin-degeneracy) at all of these k-points for the profiles with zero strain or hydrostatic strains. For the profiles with the other kinds of strains, because they are less important to the parameterization, only the eigenenergies at the three critical k-points L, Γ, and X were calculated.

Regarding the wavefunction compositions, our ETB parameterization requires the squared modules of the projections of the DFT wavefunctions onto the atomic-like orbitals with s, p, d, ... symmetries (see Eqs. (5) and (6) in the paper). However, since this information is not readily available in QuantumATK's outputs, additional mathematical treatment is needed as follows. At each k-point, the projected density of states (PDOS) $D(E)$ for a given orbital symmetry was calculated in QuantumATK using the Gaussian broadening $\sigma = 10$ meV. Then, in combination with the knowledge of N eigenenergies (at the same k-point), we have the following system of N linear equations for each kind of orbital symmetry (e.g. s_c-symmetry):

$$\begin{aligned} D^{s_c}(E_1) &= G_{1,1}|\langle s_c|\Psi_1\rangle|^2 + ... + G_{1,N}|\langle s_c|\Psi_N\rangle|^2 \\ D^{s_c}(E_2) &= G_{2,1}|\langle s_c|\Psi_1\rangle|^2 + ... + G_{2,N}|\langle s_c|\Psi_N\rangle|^2 \\ &... \\ D^{s_c}(E_N) &= G_{N,1}|\langle s_c|\Psi_1\rangle|^2 + ... + G_{N,N}|\langle s_c|\Psi_N\rangle|^2 \end{aligned}$$

where $G_{i,j} = \mathrm{e}^{-(E_i-E_j)^2/(2\sigma^2)}/(2\pi\sigma^2)$ is the Gaussian function and the squared modules of the projections $|\langle s_c|\Psi_i\rangle|^2$ $(i = 1, \ldots, N)$ are the unknowns we need to solve for. Doing similarly for the other orbital symmetries, we obtained the compositions of all DFT wavefunctions corresponding to all calculated eigenenergies. In our example of GaN parameterization, we used only the DFT wavefunction compositions at the three critical k-points L, Γ, X for the fitting, but as many k-points as needed can be included.

The Python scripts for the DFT calculations of GaN with QuantumATK as well as for extracting the DFT targets are also provided in our ETB parameterization toolbox at [75].

Appendix C: GaN parameter sets

In Table V we show the estimated values of the sp^3 parameters for the unstrained zincblende profile of GaN. Tables VI and VII show the actual $sp^3d^5s^*$ parameters for GaN that we fitted using our parameterization strategy.

TABLE V. Estimations of sp^3 parameters for unstrained zincblende profile of GaN calculated from the DFT eigenenergies at Γ and X following the steps in [14]. "Est." stands for "Estimation".

Onsite	E_{s_c}	E_{p_c}	E_{s_a}	E_{p_a}	
Est. (eV)	-2.01264	8.85579	-13.34384	2.99523	
Hopping	$V_{s_a s_c \sigma}$	$V_{s_a p_c \sigma}$	$V_{p_a s_c \sigma}$	$V_{p_a p_c \sigma}$	$V_{p_a p_c \pi}$
Est. (eV)	-2.31458	4.10657	3.08572	5.67216	-0.90473

TABLE VI. The fitted values (unitless for λs, in eV for the others) of the GaN parameters at 300 K for the onsite energies, spin-orbit couplings, band offset variation and intracouplings (following the notations in [20]). The reference bond length is $d_{\text{ref}} = 0.19622$ nm, δd is zero.

$\boldsymbol{E_{s_c}}$	$\boldsymbol{E_{p_c}}$	$\boldsymbol{E_{s_c^*}}$	$\boldsymbol{E_{d_c}}$	$\boldsymbol{\Delta_c}$
1.4880	8.6528	12.7318	13.5576	0.0243
$\boldsymbol{E_{s_a}}$	$\boldsymbol{E_{p_a}}$	$\boldsymbol{E_{s_a^*}}$	$\boldsymbol{E_{d_a}}$	$\boldsymbol{\Delta_a}$
-20.7643	4.5320	19.4300	14.1842	0.0045
$\boldsymbol{I_{s_{c,a}}}$	$\boldsymbol{I_{p_{c,a}}}$	$\boldsymbol{I_{s^*_{c,a}}}$	$\boldsymbol{I_{d_{c,a}}}$	$\boldsymbol{\Delta_{ca}}$
2.9456	4.3728	6.0053	6.2920	0.0000
$\boldsymbol{I_{s_{a,c}}}$	$\boldsymbol{I_{p_{a,c}}}$	$\boldsymbol{I_{s^*_{a,c}}}$	$\boldsymbol{I_{d_{a,c}}}$	$\boldsymbol{\Delta_{ac}}$
6.8839	2.4550	4.3555	10.6617	0.0000
$\boldsymbol{\lambda_{s_{c,a}}}$	$\boldsymbol{\lambda_{p_{c,a}}}$	$\boldsymbol{\lambda_{s^*_{c,a}}}$	$\boldsymbol{\lambda_{d_{c,a}}}$	$\boldsymbol{O}$
1.4634	1.3582	1.5771	0.9555	-3.0657
$\boldsymbol{\lambda_{s_{a,c}}}$	$\boldsymbol{\lambda_{p_{a,c}}}$	$\boldsymbol{\lambda_{s^*_{a,c}}}$	$\boldsymbol{\lambda_{d_{a,c}}}$	$\boldsymbol{\lambda_O}$
1.0309	0.9055	1.1065	2.0302	0.6178
$\boldsymbol{C_{s_c p_c,a}}$	$\boldsymbol{C_{p_c p_c,a}}$	$\boldsymbol{C_{s_c^* p_c,a}}$	$\boldsymbol{C_{p_c d_c,a}}$	$\boldsymbol{C_{d_c d_c,a}}$
1.9965	2.9987	1.2260	2.2931	2.8622
$\boldsymbol{C_{s_a p_a,c}}$	$\boldsymbol{C_{p_a p_a,c}}$	$\boldsymbol{C_{s_a^* p_a,c}}$	$\boldsymbol{C_{p_a d_a,c}}$	$\boldsymbol{C_{d_a d_a,c}}$
1.8985	1.4113	1.9991	1.6511	2.3293

TABLE VII. The fitted values (in eV) of the GaN parameters at 300 K for the intercouplings between Ga cation and N anion (following the notations in [20]). The reference bond length is $d_{\text{ref}} = 0.19622$ nm, δd is zero.

Hopping	$\boldsymbol{V}$	$\boldsymbol{\eta}$	$\boldsymbol{P}$	$\boldsymbol{S}$	$\boldsymbol{Q}$
$s_a s_c \sigma$	-3.1643	1.8086	1.8473	1.1501	0.9511
$s_a p_c \sigma$	5.4257	1.0147	-0.0001	0.0553	1.1067
$s_a s_c^* \sigma$	-3.4842	1.7856	-1.9318	2.8704	1.0081
$s_a d_c \sigma$	-6.6181	1.6501	0.1828	2.9817	-0.1728
$p_a s_c \sigma$	3.8917	1.3524	-0.0910	0.8578	0.4757
$p_a p_c \sigma$	5.9404	1.1427	-2.2018	2.9703	-2.9963
$p_a s_c^* \sigma$	0.0007	1.2228	-0.1261	1.0698	2.2125
$p_a d_c \sigma$	-3.2043	0.8668	-1.2852	2.5879	-2.5806
$s_a^* s_c \sigma$	-3.5653	1.4407	2.9995	-2.7408	0.2975
$s_a^* s_c^* \sigma$	5.2904	1.1554	-2.8393	2.9928	1.7727
$s_a^* s_c^* \sigma$	-0.0001	1.3222	2.4965	-0.6782	1.7631
$s_a^* d_c \sigma$	-3.9379	2.0987	2.9211	0.3757	-0.1125
$d_a s_c \sigma$	-0.0004	1.3353	2.9848	0.1848	-0.5041
$d_a p_c \sigma$	-0.1525	2.3547	2.0903	-0.1071	-0.6331
$d_a s_c^* \sigma$	-7.7754	2.4998	0.3276	2.8865	-0.3205
$d_a d_c \sigma$	-8.5526	2.1937	-0.0774	2.7196	2.9947
$p_a p_c \pi$	-2.2936	1.6952	0.6729	-0.1421	0.0000
$p_a d_c \pi$	2.8875	0.6597	2.6884	-1.9101	2.9930
$d_a p_c \pi$	6.8886	1.7848	-0.1391	2.4785	0.4517
$d_a d_c \pi$	7.3331	1.5381	0.6581	1.4277	2.9553
$d_a d_c \delta$	-1.3819	0.0077	2.2604	1.4651	-0.0088

Appendix D: The contributions of s^*-orbitals to the s-composition of the wavefunctions

Because the DFT calculations can give only the orbital compositions in terms of s-, p- and d-symmetry orbitals, a natural question is what to do with the contributions of s^*-orbitals in the ETB calculations. Possible choices are: (i) ignore s^*-contributions and only compare s-contributions in the ETB with that in the DFT, or (ii) sum up s- and s^*-contributions in the ETB together and compare the sum with the s-contributions in the DFT. Note that the s^* orbital can be interpreted as the s orbital of the next higher shell (right after the valence shell) in the electron configuration of the atom [14]. Thus, one probably choose the option (ii), based on the physical intuition that both s and s^* orbitals have s-symmetry and should be treated in the same way and the DFT s-composition already included the contributions from both s and s^*. In fact, we can derive a mathematical condition to test whether this is the case or not. Assuming only the s orbitals in the valence shells contribute to the DFT s-compositions of the wavefunctions, for a fair comparison between the ETB and the DFT calculations we have to use the sp^3d^5 ETB basis set, i.e. without s^*. With this basis set, the ETB Hamiltonian matrix for a zincblende crystal at Γ-point can be written in block-

diagonal form in which the s_c and s_a orbitals (c and a stand for "cation" and "anion") are decoupled from the other orbitals and together form a 2×2 matrix block (for each spin):

$$H_{s_c s_a} = \begin{pmatrix} C & V \\ V^* & A \end{pmatrix} \tag{D1}$$

where C and A are the onsite energies of s_c and s_a, respectively, while V is the coupling strength between them. One can easily analytically diagonalize this matrix block to obtain the two eigenenergies $E_\pm$ (assuming $E_- < E_+$) and two corresponding orthonormalized eigenvectors $\psi_\pm = \begin{pmatrix} c^\pm_{s_c} & c^\pm_{s_a} \end{pmatrix}^T$. The E_- energy is the lowest valence band and E_+ is the lowest conduction band at Γ-point. From the eigenvectors $\psi_\pm$, with some lengthy but simple mathematical arrangements, one can derive the following condition:

$$\frac{1}{|c^-_{s_c}|^2} + \frac{1}{|c^+_{s_c}|^2} \geq 4. \tag{D2}$$

and a similar condition for s_a. That said, if only the s orbitals in the valence shells contribute to the DFT s-compositions, then those compositions must satisfy the condition in Eq. (D2), otherwise there must be contributions from other s-symmetry orbitals, namely from s^* orbitals. We checked the DFT s-compositions at Γ-point of the zincblende GaN and found that the condition (D2) is not fulfilled. This means we can never match the s-compositions in the DFT targets by solely using the ETB s-compositions. In order to have a fair comparison, the ETB s^*-compositions must be added, as anticipated in option (ii) above.

Appendix E: A trick to speed up the convergence

The MOGA in Matlab is designed to ensure the diversity in the Pareto points, i.e., these points tend to spread over a large range in the objective space. This fact makes the algorithm slower after some iterations because it spends time on improving uninteresting points, i.e., the points that achieve a low value in one of the loss functions, but have unacceptably high value in the other. To boost the speed and guide the MOGA to focus only on the most potential points, we used the following trick (see Fig. 3 for a visualization):

1. *Stop* the current optimization cycle if there is only little improvement over many iterations;
2. Choose some cutoffs for the L^E and L^Ψ cost functions and keep only Pareto points that lie within both the cutoffs while *filtering out* all the others;
3. *Redefine* the two objectives so that if a point have L^E (or L^Ψ) cost greater than the corresponding cutoff, then multiply its L^Ψ (L^E) cost by some large number (e.g. by a factor of 10) to move this point out of the interest of MOGA;
4. *Restart* MOGA for a new cycle, this time use the filtered points as the new initial guesses (along with the randomly generated ones).

This trick can be repeated as many times as needed until the Pareto front can no longer be considerably improved.

Appendix F: Comments on fitting band offset's variation

As discussed in [10], one of the advantages of the Tan scheme with respect to the Jancu scheme is that the Tan scheme takes the band offset variation as an integrated part while the Jancu scheme does not. In the Tan scheme, the variation of the band offset is present in the determination of the diagonal Hamiltonian matrix elements via the terms $O_{i,j} \exp(-\lambda^O_{i,j} \cdot \delta)$ with $O_{i,j}$ being some pair-type-specific parameter to be fitted (see Equations (6) and (8) in [20]). Note that the movement of the valence band edge in the energy under hydrostatic strain relative to its "unstrained" position (i.e. the valence hydrostatic deformation potential) is not due only to the terms $O_{i,j} \exp(-\lambda^O_{i,j} \cdot \delta)$ but is the net result of the interplay between the distance scaling of the onsite energies, hopping energies and band offset. That is why the band offset variation must be taken in Stage 3 instead of being treated *a posteriori*. To do that, the target DFT band structures for different hydrostatic strains must supply the absolute energy values of the valence band edges with respect to the same common reference energy level.

Appendix G: Details of the supercell simulations

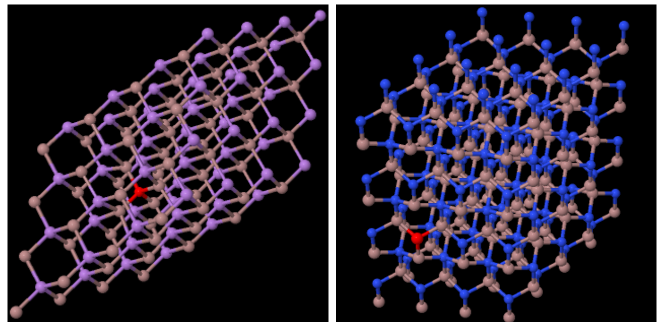

FIG. 9. Visualizations of the atomistic structures of the supercells used in our supercell simulations for the HMAs: zincblende GaP:N, GaAs:N, GaSb:N on the left; wurtzite GaN:P, GaN:As, GaN:Sb on the right. The single impurity atom is colored in red.

The supercells simulations were performed in the framework of TiberCAD [35, 36]. For each of three dilute-N zincblende HMAs, a supercell of the size $4 \times 4 \times 4$ unit cells containing 128 atoms of the host material (GaP/GaAs/GaSb) was built, then one anion (P/As/Sb)

is substituted by a N atom, resulting in a composition of %N ≈ 1.56%. Similarly, for each of three dilute-P/As/Sb wurtzite HMAs, a GaN supercell of 4 × 4 × 4 unit cells containing 256 atoms was built, then one N atom is replaced by a P/As/Sb atom, resulting in a composition of %P/%As/%Sb ≈ 0.78%. The atomistic structures of the zincblende and wurtzite HMAs are visualized in Fig. 9. We then fully relaxed the whole supercell using a simple valence force-field (VFF) method [84] before solving for its effective band structure using the Tan ETB scheme [20] and a unfolding technique described in [85]. The information about the lattice parameters and elastic constants of the parent materials in both zincblende and wurtzite phases, which is required by the VFF model in the relaxation step, was collected from [86–89] with the preference to use the experimental values where available. Moreover, the relative valence band offsets between the parent materials in zincblende phase, except GaN, were taken from [86]. For zincblende GaN, we chose a band offset of 2.1 eV below zincblende GaAs, based on the diagram in Fig. 11 of [52]. Once the band offsets between the parent materials in zincblende phase are set, the corresponding band offsets in wurtzite phase follow automatically thanks to the polytype transferability of the Tan ETB scheme.

[1] J. C. Slater and G. F. Koster, Simplified LCAO Method for the Periodic Potential Problem, Physical Review **94**, 1498 (1954).

[2] C. M. Goringe, D. R. Bowler, and E. Hernández, Tight-binding modelling of materials, Reports on Progress in Physics **60**, 1447 (1997).

[3] A. Di Carlo, Microscopic theory of nanostructured semiconductor devices: Beyond the envelope-function approximation, Semiconductor Science and Technology **18**, R1 (2003).

[4] D. A. Papaconstantopoulos and M. J. Mehl, The Slater Koster tight-binding method: A computationally efficient and accurate approach, Journal of Physics: Condensed Matter **15**, R413 (2003).

[5] A. T. Paxton, An Introduction to the Tight Binding Approximation - Implementation by Diagonalisation, in *Multiscale Simulation Methods in Molecular Sciences: Winter School, 2 - 6 March 2009, Forschungszentrum Jülich, Germany ; Lecture Notes*, NIC Series / John von Neumann Institute for Computing No. 42 (Supercomputing Centre, Forschungszentrum Jülich, Jülich, 2009).

[6] G. Klimeck and T. Boykin, Tight-Binding Models, Their Applications to Device Modeling, and Deployment to a Global Community, in *Springer Handbook of Semiconductor Devices*, edited by M. Rudan, R. Brunetti, and S. Reggiani (Springer International Publishing, Cham, 2023) pp. 1601–1640.

[7] M. Zieliński, Including strain in atomistic tight-binding Hamiltonians: An application to self-assembled InAs/GaAs and InAs/InP quantum dots, Physical Review B **86**, 115424 (2012).

[8] M. Luisier, A. Schenk, W. Fichtner, and G. Klimeck, Atomistic simulation of nanowires in the $sp^3d^5s^*$ tight-binding formalism: From boundary conditions to strain calculations, Physical Review B **74**, 205323 (2006).

[9] M. Auf der Maur, A. Pecchia, G. Penazzi, W. Rodrigues, and A. Di Carlo, Efficiency Drop in Green InGaN/GaN Light Emitting Diodes: The Role of Random Alloy Fluctuations, Physical Review Letters **116**, 027401 (2016).

[10] A.-L. Phan, A. Pecchia, A. Di Vito, and M. Auf der Maur, Empirical tight-binding method for large-supercell simulations of disordered semiconductor alloys, Physica Scripta **99**, 075903 (2024).

[11] M. Nestoklon, Tight-binding description of inorganic lead halide perovskites in cubic phase, Computational Materials Science **196**, 110535 (2021).

[12] N. Marzari, A. A. Mostofi, J. R. Yates, I. Souza, and D. Vanderbilt, Maximally localized Wannier functions: Theory and applications, Reviews of Modern Physics **84**, 1419 (2012).

[13] A. Ghosh, A. M. Schankler, and A. M. Rappe, Choosing tight-binding models for accurate optoelectronic responses, Physical Review B **111**, 125203 (2025).

[14] P. Vogl, H. P. Hjalmarson, and J. D. Dow, A Semi-empirical tight-binding theory of the electronic structure of semiconductors†, Journal of Physics and Chemistry of Solids **44**, 365 (1983).

[15] J.-M. Jancu, R. Scholz, F. Beltram, and F. Bassani, Empirical spds* tight-binding calculation for cubic semiconductors: General method and material parameters, Physical Review B **57**, 6493 (1998).

[16] O. Madelung, *Semiconductors: Data Handbook*, 3rd ed. (Springer Berlin Heidelberg, Berlin, Heidelberg, 2004).

[17] P.-O. Löwdin, On the Non-Orthogonality Problem Connected with the Use of Atomic Wave Functions in the Theory of Molecules and Crystals, The Journal of Chemical Physics **18**, 365 (1950).

[18] G. L. Bir and G. E. Pikus, *Symmetry and Strain-Induced Effects in Semiconductors* (Wiley, New York, 1974).

[19] M. A. Caro, S. Schulz, and E. P. O'Reilly, Theory of local electric polarization and its relation to internal strain: Impact on polarization potential and electronic properties of group-III nitrides, Physical Review B **88**, 214103 (2013).

[20] Y. Tan, M. Povolotskyi, T. Kubis, T. B. Boykin, and G. Klimeck, Transferable tight-binding model for strained group IV and III-V materials and heterostructures, Physical Review B **94**, 045311 (2016).

[21] J.-M. Jancu and P. Voisin, Tetragonal and trigonal deformations in zinc-blende semiconductors: A tight-binding point of view, Physical Review B **76**, 115202 (2007).

[22] J.-M. Jancu, F. Bassani, F. D. Sala, and R. Scholz, Transferable tight-binding parametrization for the group-III nitrides, Applied Physics Letters **81**, 4838 (2002).

[23] F. Raouafi, R. Benchamekh, M. O. Nestoklon, J.-M. Jancu, and P. Voisin, Intrinsic interface states in InAs–AlSb heterostructures, Journal of Physics: Condensed Matter **28**, 045001 (2016).

[24] M. O. Nestoklon, R. Benchamekh, and P. Voisin, Virtual crystal description of III–V semiconductor alloys in the

tight binding approach, Journal of Physics: Condensed Matter **28**, 305801 (2016).

[25] T. B. Boykin, G. Klimeck, R. C. Bowen, and F. Oyafuso, Diagonal parameter shifts due to nearest-neighbor displacements in empirical tight-binding theory, Physical Review B **66**, 125207 (2002).

[26] Y. M. Niquet, D. Rideau, C. Tavernier, H. Jaouen, and X. Blase, Onsite matrix elements of the tight-binding Hamiltonian of a strained crystal: Application to silicon, germanium, and their alloys, Physical Review B **79**, 245201 (2009).

[27] T. B. Boykin, M. Luisier, M. Salmani-Jelodar, and G. Klimeck, Strain-induced, off-diagonal, same-atom parameters in empirical tight-binding theory suitable for [110] uniaxial strain applied to a silicon parametrization, Physical Review B **81**, 125202 (2010).

[28] T.-X. Liu, M.-E. Pistol, C. Pryor, and L. Mao, Speeding up tight binding calculations using zone-folding methods, Computational Materials Science **211**, 111479 (2022).

[29] Y. Tan, M. Povolotskyi, T. Kubis, Y. He, Z. Jiang, G. Klimeck, and T. B. Boykin, Empirical tight binding parameters for GaAs and MgO with explicit basis through DFT mapping, Journal of Computational Electronics **12**, 56 (2013).

[30] Y. P. Tan, M. Povolotskyi, T. Kubis, T. B. Boykin, and G. Klimeck, Tight-binding analysis of Si and GaAs ultrathin bodies with subatomic wave-function resolution, Physical Review B **92**, 085301 (2015).

[31] To compare the wavefunctions, the DFT wavefunctions are projected onto the orthogonalized atomic-like basis set to obtain the DFT expansion coefficients. Then those expansion coefficients will be compared with the ETB ones.

[32] Gamultiobj Algorithm - MATLAB & Simulink, https://www.mathworks.com/help/gads/gamultiobj-algorithm.html.

[33] The MOGA of MATLAB® is much more convenient, robust and efficient than an user-implemented version. The parallelization to speed up the algorithm can also be enabled easily.

[34] S. Smidstrup, T. Markussen, P. Vancraeyveld, J. Wellendorff, J. Schneider, T. Gunst, B. Verstichel, D. Stradi, P. A. Khomyakov, U. G. Vej-Hansen, M.-E. Lee, S. T. Chill, F. Rasmussen, G. Penazzi, F. Corsetti, A. Ojanperä, K. Jensen, M. L. N. Palsgaard, U. Martinez, A. Blom, M. Brandbyge, and K. Stokbro, QuantumATK: An integrated platform of electronic and atomic-scale modelling tools, Journal of Physics: Condensed Matter **32**, 015901 (2020).

[35] M. Auf der Maur, M. Povolotskyi, F. Sacconi, and A. Di Carlo, TiberCAD: A new multiscale simulator for electronic and optoelectronic devices, Superlattices and Microstructures **41**, 381 (2007).

[36] M. Auf Der Maur, M. Povolotskyi, F. Sacconi, A. Pecchia, G. Romano, G. Penazzi, and A. Di Carlo, TiberCAD: Towards multiscale simulation of optoelectronic devices, Optical and Quantum Electronics **40**, 1077 (2008).

[37] We chose to use the "Fitted" columns, but one can use "Analytical" column without much differences, noting that this is just for rough estimations.

[38] E. Hellinger, Neue Begründung der Theorie quadratischer Formen von unendlichvielen Veränderlichen., Journal für die reine und angewandte Mathematik **1909**, 210 (1909).

[39] X. H. Lu, P. Y. Yu, L. X. Zheng, S. J. Xu, M. H. Xie, and S. Y. Tong, Evidence for a Type-II band alignment between cubic and hexagonal phases of GaN, Applied Physics Letters **82**, 1033 (2003).

[40] S. K. Bhattacharya, P. A. Deodhar, R. Viswanatha, and A. Kshirsagar, Transferable orthogonal tight-binding parameters for ZnS and CdS, Journal of Physics: Condensed Matter **22**, 295304 (2010).

[41] J. Sink and C. Pryor, Empirical tight-binding parameters for wurtzite group III–V(non-nitride) and IV materials, AIP Advances **13**, 025354 (2023).

[42] N. Vainorius, S. Lehmann, D. Jacobsson, L. Samuelson, K. A. Dick, and M.-E. Pistol, Confinement in Thickness-Controlled GaAs Polytype Nanodots, Nano Letters **15**, 2652 (2015).

[43] B. Loitsch, M. Müller, J. Winnerl, P. Veit, D. Rudolph, G. Abstreiter, J. J. Finley, F. Bertram, J. Christen, and G. Koblmüller, Microscopic nature of crystal phase quantum dots in ultrathin GaAs nanowires by nanoscale luminescence characterization, New Journal of Physics **18**, 063009 (2016).

[44] M. Spies and E. Monroy, Nanowire photodetectors based on wurtzite semiconductor heterostructures, Semiconductor Science and Technology **34**, 053002 (2019).

[45] S. Lehmann, D. Jacobsson, K. Deppert, and K. A. Dick, High crystal quality wurtzite-zinc blende heterostructures in metal-organic vapor phase epitaxy-grown GaAs nanowires, Nano Research **5**, 470 (2012).

[46] J. Sink and C. Pryor, Wurtzite/Zincblende Crystal Phase GaAs Heterostructures in the Tight Binding Approximation, Physical Review B **108**, 075104 (2023).

[47] L. S. Ramsdell, Studies on silicon carbide, American Mineralogist **32**, 64 (1947).

[48] G. Lehmann and M. Taut, On the Numerical Calculation of the Density of States and Related Properties, physica status solidi (b) **54**, 469 (1972).

[49] P. E. Blöchl, O. Jepsen, and O. K. Andersen, Improved tetrahedron method for Brillouin-zone integrations, Physical Review B **49**, 16223 (1994).

[50] R. Kudrawiec and D. Hommel, Bandgap engineering in III-nitrides with boron and group V elements: Toward applications in ultraviolet emitters, Applied Physics Reviews **7**, 041314 (2020).

[51] K. M. Yu, S. V. Novikov, R. Broesler, I. N. Demchenko, J. D. Denlinger, Z. Liliental-Weber, F. Luckert, R. W. Martin, W. Walukiewicz, and C. T. Foxon, Highly mismatched crystalline and amorphous $GaN_{1-x}As_x$ alloys in the whole composition range, Journal of Applied Physics **106**, 103709 (2009).

[52] K. M. Yu, S. V. Novikov, M. Ting, W. L. Sarney, S. P. Svensson, M. Shaw, R. W. Martin, W. Walukiewicz, and C. T. Foxon, Growth and characterization of highly mismatched $GaN_{1-x}Sb_x$ alloys, Journal of Applied Physics **116**, 123704 (2014).

[53] W. Walukiewicz and J. M. O. Zide, Highly Mismatched Semiconductor Alloys: From Atoms to Devices, Journal of Applied Physics **127**, 010401 (2020).

[54] C. A. Broderick, M. Usman, S. J. Sweeney, and E. P. O'Reilly, Band engineering in dilute nitride and bismide semiconductor lasers, Semiconductor Science and Technology **27**, 094011 (2012).

[55] W. Shan, W. Walukiewicz, J. W. Ager, E. E. Haller, J. F. Geisz, D. J. Friedman, J. M. Olson, and S. R. Kurtz,

Band Anticrossing in GaInNAs Alloys, Physical Review Letters **82**, 1221 (1999).

[56] W. Shan, W. Walukiewicz, K. Yu, J. Ager III, E. Haller, J. Geisz, D. Friedman, J. Olson, S. Kurtz, H. Xin, and C. Tu, Band Anticrossing in III-N-V Alloys, physica status solidi (b) **223**, 75 (2001).

[57] J. Wu, W. Shan, and W. Walukiewicz, Band anticrossing in highly mismatched III V semiconductor alloys, Semiconductor Science and Technology **17**, 860 (2002).

[58] W. Shan, W. Walukiewicz, K. M. Yu, J. Wu, J. W. Ager, E. E. Haller, H. P. Xin, and C. W. Tu, Nature of the fundamental band gap in GaN_xP_{1-x} alloys, Applied Physics Letters **76**, 3251 (2000).

[59] J. Wu, W. Walukiewicz, K. M. Yu, J. W. Ager, E. E. Haller, Y. G. Hong, H. P. Xin, and C. W. Tu, Band anticrossing in $GaP_{1-x}N_x$ alloys, Physical Review B **65**, 241303 (2002).

[60] P. H. Jefferson, T. D. Veal, L. F. J. Piper, B. R. Bennett, C. F. McConville, B. N. Murdin, L. Buckle, G. W. Smith, and T. Ashley, Band anticrossing in GaN_xSb_{1-x}, Applied Physics Letters **89**, 111921 (2006).

[61] M. P. Polak, R. Kudrawiec, and O. Rubel, Electronic band structure of nitrogen diluted Ga(PAsN): Formation of the intermediate band, direct and indirect optical transitions, and localization of states, Journal of Applied Physics **126**, 10.1063/1.5097977 (2019).

[62] Q. Meng, S. R. Bank, and M. A. Wistey, Undoing band anticrossing in highly mismatched alloys by atom arrangement, Journal of Applied Physics **135**, 113101 (2024).

[63] J. Ziembicki, R. Bartoszewicz, M. Grodzicki, P. Scharoch, R. Kudrawiec, W. Olszewski, D. Pucicki, D. Hommel, and M. P. Polak, Electronic band structure of GaN diluted and overdiluted with group-V elements, Physical Review Applied **23**, 024005 (2025).

[64] V. Virkkala, V. Havu, F. Tuomisto, and M. J. Puska, Hybrid functional study of band structures of $GaAs_{1-x}N_x$ and $GaSb_{1-x}N_x$ alloys, Physical Review B **85**, 10.1103/physrevb.85.085134 (2012).

[65] I. A. Buyanova, M. Izadifard, A. Kasic, H. Arwin, W. M. Chen, H. P. Xin, Y. G. Hong, and C. W. Tu, Analysis of band anticrossing in GaN_xP_{1-x} alloys, Physical Review B **70**, 10.1103/physrevb.70.085209 (2004).

[66] U. Tisch, E. Finkman, and J. Salzman, The anomalous bandgap bowing in GaAsN, Applied Physics Letters **81**, 463 (2002).

[67] T. D. Veal, L. F. J. Piper, S. Jollands, B. R. Bennett, P. H. Jefferson, P. A. Thomas, C. F. McConville, B. N. Murdin, L. Buckle, G. W. Smith, and T. Ashley, Band gap reduction in GaNSb alloys due to the anion mismatch, Applied Physics Letters **87**, 132101 (2005).

[68] H. Y. Huang, C. H. Chuang, C. K. Shu, Y. C. Pan, W. H. Lee, W. K. Chen, W. H. Chen, and M. C. Lee, Photoluminescence and photoluminescence excitation studies of as-grown and P-implanted GaN: On the nature of yellow luminescence, Applied Physics Letters **80**, 3349 (2002).

[69] S. Novikov, A. Winser, A. Bell, I. Harrison, T. Li, R. Campion, C. Staddon, C. Davis, F. Ponce, and C. Foxon, The transition from As-doped GaN, showing blue emission, to GaNAs alloys in films grown by molecular beam epitaxy, Journal of Crystal Growth **240**, 423 (2002).

[70] J. Wu, W. Walukiewicz, K. M. Yu, J. D. Denlinger, W. Shan, J. W. Ager, A. Kimura, H. F. Tang, and T. F. Kuech, Valence band hybridization in N-rich $GaN_{1-x}As_x$ alloys, Physical Review B **70**, 115214 (2004).

[71] N. Segercrantz, K. M. Yu, M. Ting, W. L. Sarney, S. P. Svensson, S. V. Novikov, C. T. Foxon, and W. Walukiewicz, Electronic band structure of highly mismatched $GaN_{1-x}Sb_x$ alloys in a broad composition range, Applied Physics Letters **107**, 142104 (2015).

[72] S. J. Calero-Barney, A. N. Andriotis, M. Menon, and M. Sunkara, Plasma-assisted vapor liquid phase epitaxial growth of dilute $GaSb_xN_{1-x}$ and $GaBi_yN_{1-y}$ alloys: Confirmation of band gap reduction discontinuity, Physical Review B **105**, 10.1103/physrevb.105.085307 (2022).

[73] D. Soccodato, G. Penazzi, A. Pecchia, A.-L. Phan, and M. Auf Der Maur, Machine learned environment-dependent corrections for a spds* empirical tight-binding basis, Machine Learning: Science and Technology **5**, 025034 (2024).

[74] C. A. Broderick, E. P. O'Reilly, and S. Schulz, Perspective: Theory and simulation of highly mismatched semiconductor alloys using the tight-binding method, Journal of Applied Physics **135**, 100902 (2024).

[75] A parameterizer for empirical tight-binding calculations, https://github.com/tiberlab/ETB_parameterizer (2025).

[76] Uptight, https://github.com/tiberlab/uptight (2025).

[77] M. C. Muñoz and G. Armelles, X-point deformation potentials of III-V semiconductors in a tight-binding approach, Physical Review B **48**, 2839 (1993).

[78] C. Tserbak, H. M. Polatoglou, and G. Theodorou, Unified approach to the electronic structure of strained Si/Ge superlattices, Physical Review B **47**, 7104 (1993).

[79] J. L. Mercer and M. Y. Chou, Tight-binding model with intra-atomic matrix elements, Physical Review B **49**, 8506 (1994).

[80] G. Grosso and C. Piermarocchi, Tight-binding model and interactions scaling laws for silicon and germanium, Physical Review B **51**, 16772 (1995).

[81] C. Z. Wang, B. C. Pan, and K. M. Ho, An environment-dependent tight-binding potential for Si, Journal of Physics: Condensed Matter **11**, 2043 (1999).

[82] J. Heyd, G. E. Scuseria, and M. Ernzerhof, Hybrid functionals based on a screened Coulomb potential, The Journal of Chemical Physics **118**, 8207 (2003).

[83] M. Van Setten, M. Giantomassi, E. Bousquet, M. Verstraete, D. Hamann, X. Gonze, and G.-M. Rignanese, The PseudoDojo: Training and grading a 85 element optimized norm-conserving pseudopotential table, Computer Physics Communications **226**, 39 (2018).

[84] D. Camacho and Y. Niquet, Application of Keating's valence force field model to non-ideal wurtzite materials, Physica E: Low-dimensional Systems and Nanostructures **42**, 1361 (2010).

[85] M. Farjam, Projection operator approach to unfolding supercell band structures (2015), arXiv:1504.04937 [cond-mat].

[86] I. Vurgaftman, J. R. Meyer, and L. R. Ram-Mohan, Band parameters for III–V compound semiconductors and their alloys, Journal of Applied Physics **89**, 5815 (2001).

[87] I. Vurgaftman and J. R. Meyer, Band parameters for nitrogen-containing semiconductors, Journal of Applied Physics **94**, 3675 (2003).

[88] M. I. McMahon and R. J. Nelmes, Observation of a Wurtzite Form of Gallium Arsenide, Physical Review Letters **95**, 215505 (2005).

[89] J. Ziembicki, P. Scharoch, M. P. Polak, M. Wiśniewski, and R. Kudrawiec, Band parameters of group III–V semiconductors in wurtzite structure, Journal of Applied Physics **132**, 225701 (2022).